Chapter 7

Monte Carlo

Monte Carlo techniques [RC04] are of great importance for the design and interpretation of experiments in nuclear and particle physics. They offer a possibility to simulate the behavior of physical systems and the response of detectors, and to verity analysis algorithms. In the analysis presented here, Monte Carlo methods were used to determine the Coulomb correction and to understand the impact of the experimental resolution of the HBT radii.

The full CERES Monte Carlo [Slı03, Yur06] is too slow to offer a sufficient statistics in a reasonable time scale for calculation of the two-particle correlation functions discussed in this dissertation. Therefore, a simple fast generator was created, which describes the Bose-Einstein correlations and the Coulomb interactions between particles, was used instead. The generated tracks were described by the four-vectors of the momenta and the positions. The source position of the track was generated according to a three dimensional Gaussian distribution in the rest frame of the pair with the width adjusted to fit the experimental HBT radii. The momentum of the generated track was sampled from a two-dimensional histogram of the experimental momentum vs. the polar angle, reflecting the acceptance of the CERES spectrometer (see Fig. 7.1). The azimuthal angle of the track was generated from an uniform distribution in the range of $(-\pi, \pi)$. In order to minimize the time necessary for accumulation of the required statistics the second track from a pair was generated within ± 0.2 rad of the first one. In contrast to the full CERES Monte Carlo the details of the single track efficiency were ignored; the single track efficiency cancels when normalizing to the event mixing.

In the three dimensional Gaussian, sampled to generate the position, the x, y, and z dimensions were related to R_{out}, R_{side}, and R_{long}, respectively. Therefore, the generated source positions of tracks were rotated according to

$$\begin{aligned} x' &= x \cdot \cos\left(\phi_{pair}\right) - y \cdot \sin\left(\phi_{pair}\right) \ , \\ y' &= y \cdot \cos\left(\phi_{pair}\right) + x \cdot \sin\left(\phi_{pair}\right) \ , \end{aligned} \tag{7.1}$$

where ϕ_{pair} corresponds to the orientation of the transverse pair momentum vector in the lab-

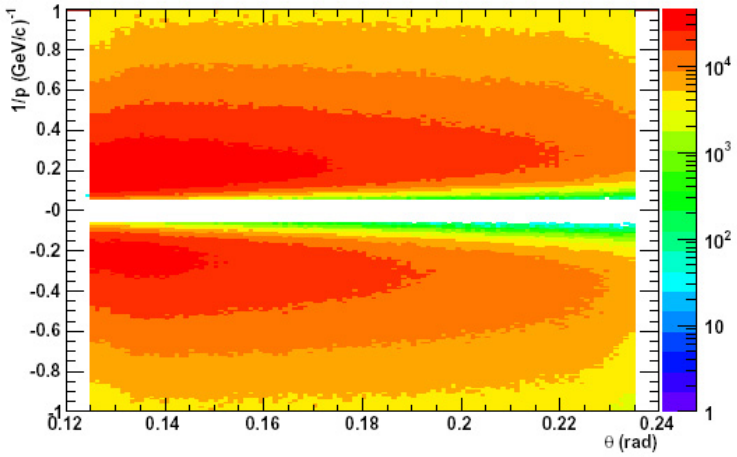

Figure 7.1: The distribution of tracks as a function of the inverse momentum and the θ angle obtained from the simulations.

oratory system. For each generated pair the Coulomb factor was calculated based on the quantum-mechanical description explained in Section 1.3.3. The HBT effect was embedded into the simulated correlation functions through the weight factors

$$C_{HBT} = 1 + \cos\left(\Delta E \cdot \Delta t - \overrightarrow{q} \cdot \overrightarrow{\Delta r}\right) , \tag{7.2}$$

where ΔE, Δt, and $\overrightarrow{\Delta r}$ are the differences between the energies, the times, and the positions of the two tracks in a pair, respectively. The histograms for the signal distributions were filled with the weights described by a product of the HBT and the Coulomb correlation functions, and with the Coulomb weight factors for the identical and the non-identical two-particle correlations, respectively. The obtained correlation functions were subject to the analysis chain allowing to test the algorithms used. Moreover, based on the generated correlation functions different corrections to the measured correlation functions were derived as it is described in the following sections.

7.1 Coulomb Correlation Functions

The Coulomb interaction between the like-sign charge particles for small relative momenta significantly influences the Bose-Einstein correlations. The Coulomb correlation functions $C_{2,C}\left(q_{inv}\right)$ were calculated based on the fast generator by averaging the Coulomb wave function squared over a spherical Gaussian source with $\sigma_t = 0$. This procedure was repeated for different Gaussian source sizes in bins of 0.5 fm. Examples of Coulomb correlation functions are shown in Fig. 7.2. These correlation functions were then used in the fit to the experimental identical pion correlation functions as described is Section 5.5.

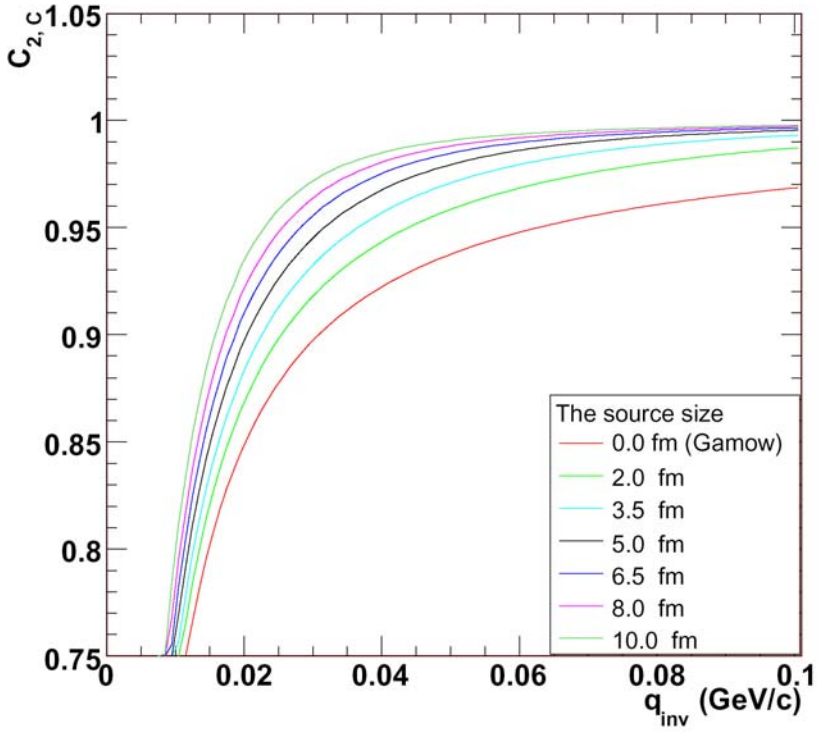

Figure 7.2: Coulomb correlation functions for different source sizes.

7.2 Momentum Resolution Influence on HBT Radii

The limited accuracy of the momentum reconstruction in the TPC, as discussed in Section 4.4, affects the measured correlation functions in the following way. The reconstructed momenta of the particles in a pair will differ from the real momenta of the particles by $\Delta\overrightarrow{p}_{1,2}$, where the index corresponds to a given particle in the pair. The peaks in the correlation functions will be lowered and broadened because of that. The broadening will lead to underestimating the HBT radii. The spatial resolution of the track can also significantly influence the measured HBT radii as it enters to calculation of the relative pair momentum via the emission angle. The effect of the finite momentum resolution was studied using the fast generator described above. The reconstructed momenta were smeared according to Eq. 4.2. The simulated angles of tracks were smeared with the momentum dependent widths of the θ and the ϕ angles derived from the matching parameterization described in Section 4.6. In Fig. 7.3 the results of three methods of estimating a correction factor for R_{out} are presented. The simplest one depicted, as a solid black line, is based on the ratio between the two correlation functions obtained for the case of infinitely good (real) and experimental (meas) momentum resolution, respectively. This method allows to extract a correct factor only if the true HBT radius is known. The second method, depicted as dash curves, assume that the momentum resolution will broaden

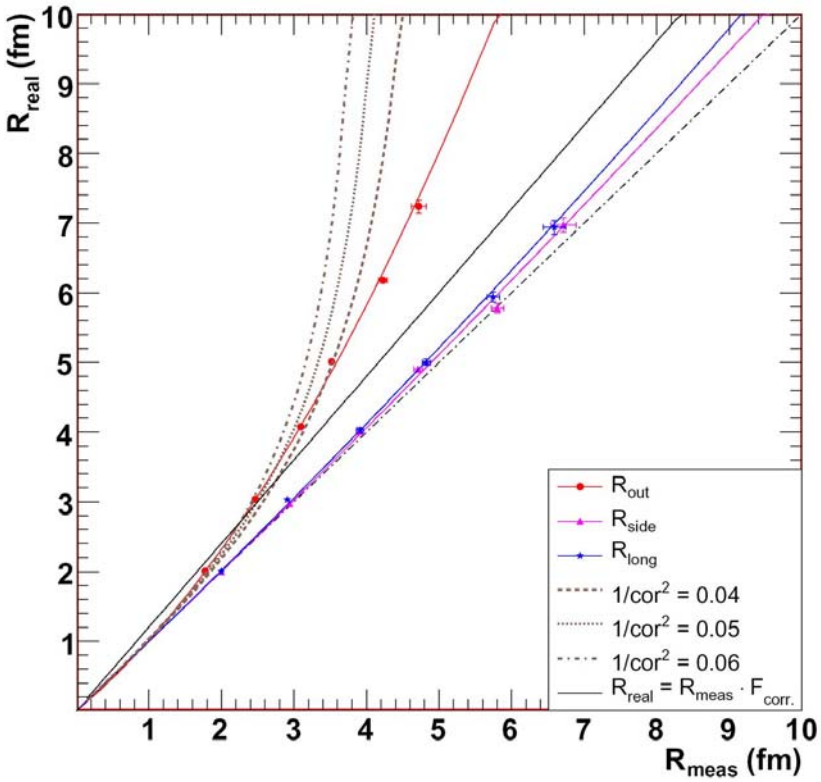

Figure 7.3: Comparison between different ways to remove the effect of the finite momentum resolution of detector on the HBT radii (pair $P_\perp$ from 1 to 2 GeV/c).

the measured correlation functions by quadratically adding a constant term to the width. The relation between true radii and measured ones can by expressed be

$$\frac{1}{R^2_{real}} = \frac{1}{R^2_{meas}} + \frac{1}{corr^2}\,. \tag{7.3}$$

The best method of calculating the correction is based on the simulation of the two-particle correlation functions for real and measured case, respectively, for different source sizes. The dependence of R_{meas} is plotted as a function of R_{real} and then parameterized with a polynomial of second order. The simulated smeared radii R_{meas} as a function of the true radii are shown in Fig. 7.4 for different $P_\perp$ bins. The worst resolution is obtained for the R_{out} radii which is dominated by pairs with small opening angle, with q_{out} given by the difference of the length of the momentum vectors. Therefore, the q_{out} component is directly sensitive to the momentum resolution and becomes more affected for increasing $P_\perp$ since the momentum resolution is proportional to the p^2. The influence of the detector resolution on the other two components of $\overrightarrow{q}$ is less significant. The q_{side} is mainly determined by the opening angle between the two particles in pair. In the case of q_{long} the effect is reduced by boosting the pair from the

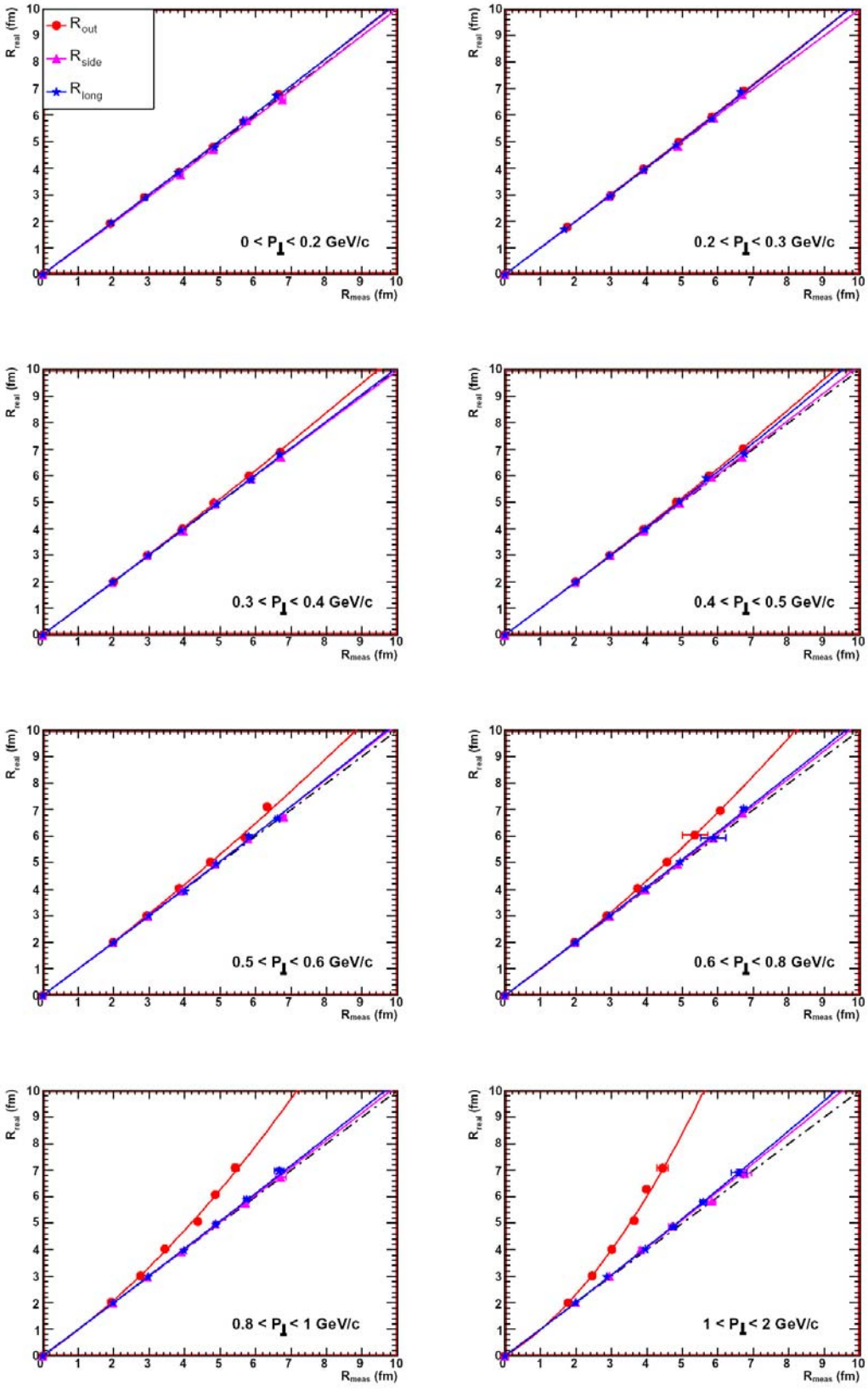

Figure 7.4: The influence of the finite momentum resolution on the measured $\pi^- - \pi^-$HBT radii.

laboratory to the LCMS reference frame. All three radii were corrected using the polynomial parametrization described above.

7.3 Reaction Plane Resolution Influence on HBT Radii

The influence of the reaction plane resolution on the HBT radii, in the case of the azimuthally sensitive analysis, was studied based on the fast generator. The finite reaction plane resolution and the finite width of the $\phi_{pair} - \Psi_2$ bins reduce the measured oscillation amplitudes of HBT radii. Before these effects can be corrected for the reaction plane resolution must be known. The latter was studied using two methods and the results are presented in Section 4.7.3. In order to better understand the different variables used to present the results of the reaction plane resolution a simple generator of the reaction plane orientation was used. The reaction plane orientation angle was sampled from an uniform distribution within $\left(-\frac{\pi}{2}, \frac{\pi}{2}\right)$. To simulate the subevent method, the two subevent reaction plane angles were calculated by smearing the original one according to Gaussian distribution with corresponding width, and the $\Psi_{SE2} - \Psi_{SE1}$ difference was calculated. The latter was used to calculate Eq. 4.19; at the same time the $dN/d(\Psi_{SE2} - \Psi_{SE1})$ distribution was filled. From the obtained distribution the $\frac{offset}{peak}$ ratio was calculated. In Fig. 7.5 both variables are plotted as a function of the reaction plane angular resolution expressed in degrees, providing a direct conversion between the variables used. Moreover, results of the experimental reaction plane resolution for different centrality classes are shown as black triangles in both plots. The σ_{RP} values of the points were taken

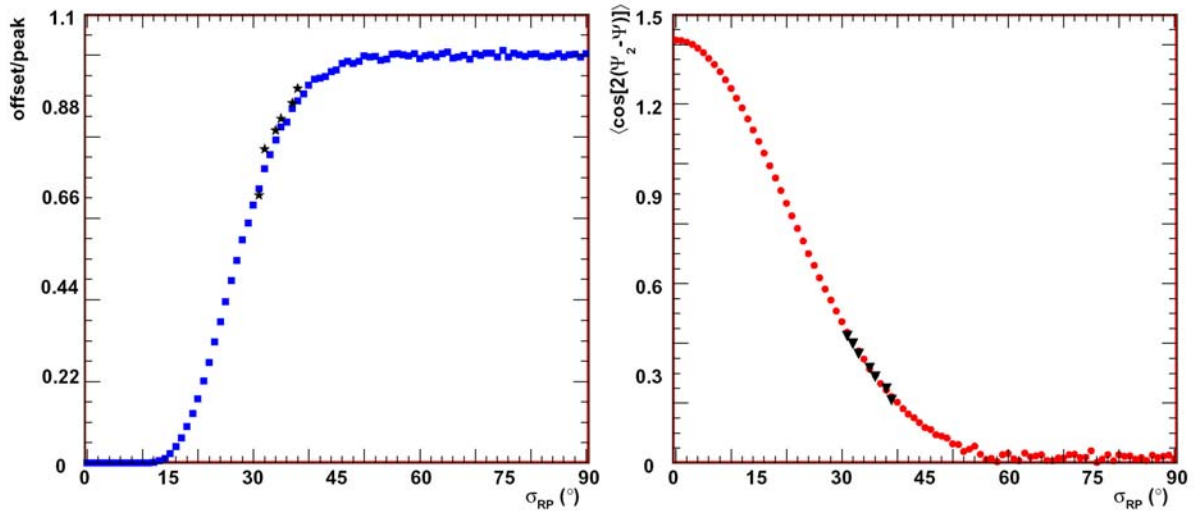

Figure 7.5: The simulation of the reaction plane resolution. The black symbols represent the reaction plane resolution of the CERES experiment.

from the width of Gaussian, fitted to the $dN/d(\Psi_{SE2} - \Psi_{SE1})$ distributions. The obtained angular resolution varies with the centrality between 31-39°.

The azimuthal dependence of the Hanbury-Brown Twiss radii was introduced into the generator based on the tilted source model proposed in [LHW00]. The generated source position of the track was rotated according to

$$\begin{aligned} x'' &= x' \cdot \cos(\Psi_2') - y' \cdot \sin(\Psi_2') \ , \\ y'' &= y' \cdot \cos(\Psi_2') + x' \cdot \sin(\Psi_2') \ , \end{aligned} \tag{7.4}$$

where Ψ_2' is the generated angle of the reaction plane orientation, and $\langle x'^2 \rangle < \langle y'^2 \rangle$. This introduces a dependence of the generated radii on orientation of pairs with respect to the reaction plane. Within this model a consistent cross-check of the analysis algorithms was performed. Furthermore, the influence of the finite event plane resolution on the HBT radii was studied based on the generated correlation functions. In this method, it is expected that the oscillations of the radii are reduced due to the finite resolution of the event plane and the effect is studied by forming a superposition of sources misaligned to the generated event plane. One should note that this method treats the longitudinal radius as being $\phi_{pair} - \Psi_2$ independent. Moreover, it neglects the finite binning of the data in reaction plane orientation. The effect of such assumption will be discussed in Section 8.2.

The correlation radii generated from the constant source size ($R_x = 4$ fm, $R_y = 5$ fm, and $R_z = 7$ fm) derived for three different values of the reaction plane resolution are shown in Fig. 7.6. The radii unaffected by the event plane resolution ($RP_{res} = 0°$) are depicted as the full circles. The fit to the data is the sine (cosine) in the case of HBT radii (cross-terms). Two extreme cases of the event plane resolution, measured by the CERES experiment, are depicted as the open circles in the case of peripheral collisions $(30 - 40\,\%\,\sigma_{GEOM})$ and the full triangles depicted the results obtained for the central collisions $(0 - 2.5\,\%\,\sigma_{GEOM})$. From the fits results the correction factor $R_{smear}/R_{perf.}$ can be derived as the amplitude ratio between the HBT radii with and without event plane resolution. In Fig. 7.7 the derived values of the $R_{smear}/R_{perf.}$ ratio as a function of the reaction plane resolution are shown for three component of the Gaussian parametrization. The results obtained for the R_{out} (left panel), the R_{side} (middle panel), and the $R_{out-side}$ (right panel) were parameterized by the first order polynomial as depicted by the green line. While this parameterization does not describe results for $\langle \cos(n\Delta\Psi) \rangle$ larger then 0.8, it still seems to be realistic for the range of the reaction plane resolution measured by the CERES spectrometer. Therefore, the three components of the azimuthally sensitive Bertsch–Pratt parameterization were corrected with the factors derived from such parameterization.

As explained above, such intuitive procedure of the event plane resolution correction neglects all effects connected with the finite bin width used for the two-particle correlations analysis. The smearing of the correlation function by imperfect event plane reconstruction is expected to diminish the amplitudes of the oscillations in the transverse radii but the effect it has on a correlation function is truely present in the individual bins of the separate histograms from

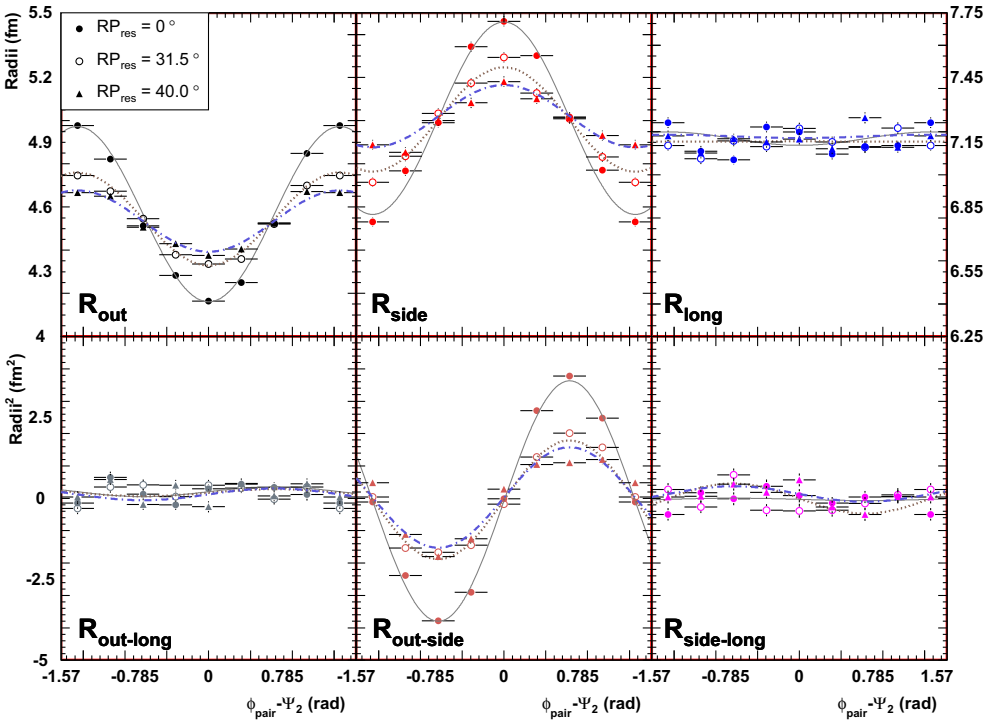

Figure 7.6: The influence of the reaction plane resolution on the HBT radii. The solid, dotted, and dash-dotted lines are fits to the three data sets.

the real and mixed pair distributions. The model-independent correction procedure proposed in [HHLW02] might be more appropriate. The effect of auto-correlation contributions to Ψ_2 was neglected during the analysis presented in this dissertation since this effect was found to be insignificant by the STAR experiment in [Col04].

7.4 Asymmetry of the Correlation and the Source Displacement

The measured non-identical two-particle correlation functions were parameterized using Eq. 6.2. The derived asymmetry parameter $\mathcal{A}$ must be converted to distance before it can be compared to theoretical calculations. The relation between the source displacement and the asymmetry was studied using the fast generator explained at the beginning of this chapter. The shift between the pion and proton source positions was introduced by shifting proton freeze-out points

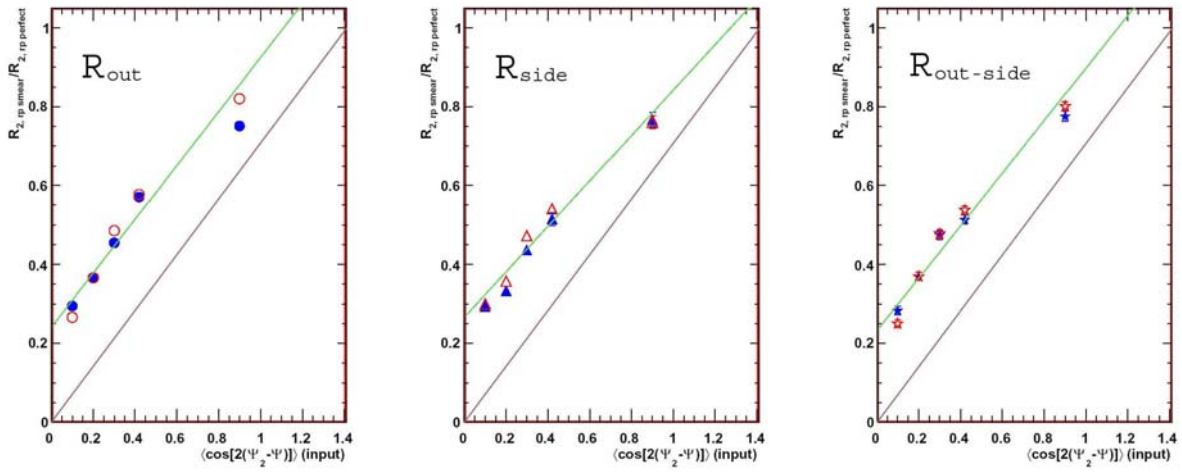

Figure 7.7: Correction factor for the reaction plane angular resolution. The full and the open symbols represent correction factors derived for the $\pi^-\pi^-$ and $\pi^+\pi^+$ correlation functions respectively.

by ΔR in the direction of the transverse pair momentum

$$\begin{aligned} x'' &= x' + \left(\frac{P_x}{P_\perp}\right) \cdot \Delta R\,, \\ y'' &= y' + \left(\frac{P_y}{P_\perp}\right) \cdot \Delta R\,, \end{aligned} \tag{7.5}$$

where ΔR is the shift, (P_x, P_y) is the pair transverse momentum, and $P_\perp = \sqrt{P_x^2 + P_y^2}$. Successively, the Coulomb weight factor was calculated and the histograms were filled, one with the Coulomb weight and the other with weight equal to one. The ratio of these two histograms was treated in the same way as the experimental correlation function yielding the asymmetry parameters $\mathcal{A}$ as a function of the transverse pair momentum. At the same time, the influence of the momentum resolution and of the finite source size, as well as of the source rapidity, were studied. In Fig. 7.8 the impact of the momentum resolution on the asymmetry parameter is shown. The momentum of particles was smeared in the same manner as in the case of the identical two-particle correlations analysis. The finite momentum resolution diminishes the asymmetry, especially at a high pair transverse momentum. The influence of the momentum resolution was taken into account during the conversion from the $\mathcal{A}$ parameter to distance. The impact of the source size on the asymmetry parameter for the $P_\perp$ independent 6 fm displacement between pions and protons average source position is shown in Fig. 7.9. The simulated correlation functions had similar source size as the one measured in experiment. Until now, all considerations were based on the assumption of the emission source sitting at midrapidity. This assumption significantly simplifies the analysis but it does not reflect the physical situation during the heavy ion collisions. The influence of the static source hypothesis was studied by

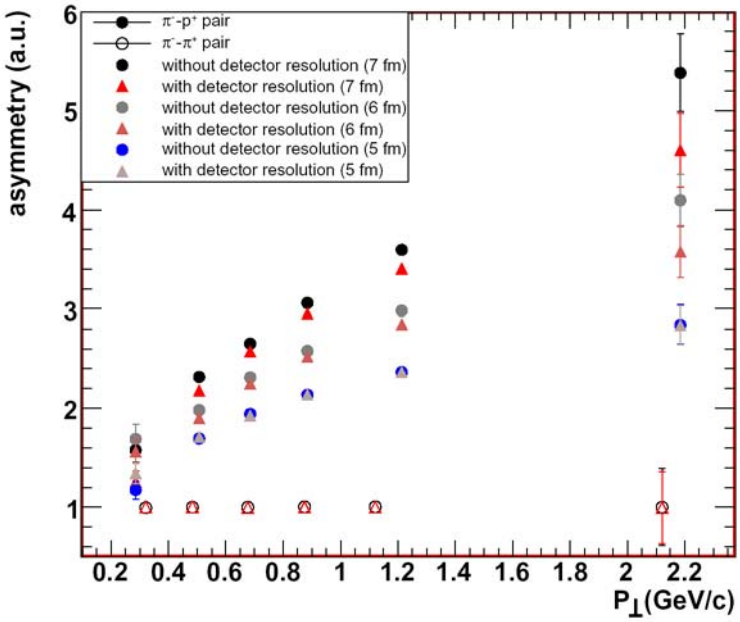

Figure 7.8: The momentum resolution influence on the asymmetry of the unlike particles correlation functions.

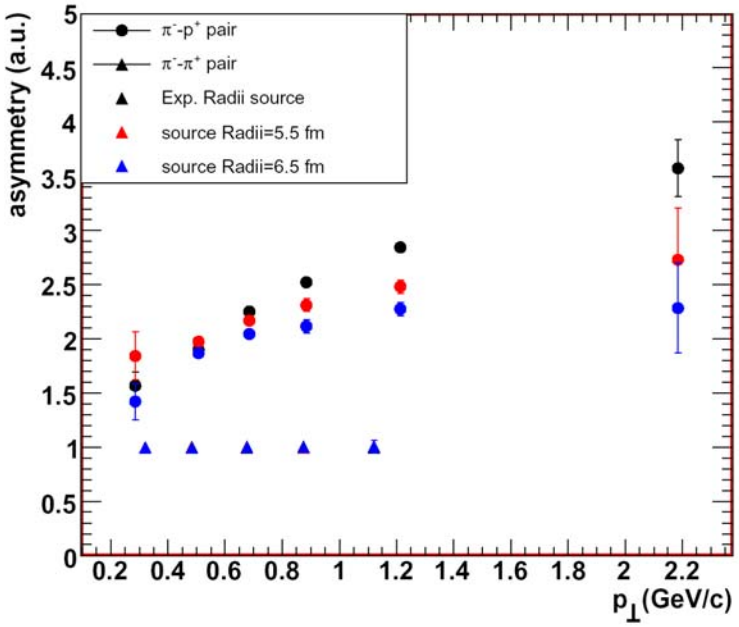

Figure 7.9: The asymmetry parameter dependence on the source radii as a function of $P_{\perp}$.

boosting the generated positions in the longitudinal and transverse directions (Fig. 7.10). The results were used to estimate the maximum systematic error of the analysis.

In Fig. 7.11 the values of the $\mathcal{A}$ parameters as a function of the displacement in steps of 1 fm are shown for the six bins of $P_\perp$. For symmetry reasons all curves should go through (0,1). However, due to the limited acceptance of the CERES spectrometer, in the case of the pion-proton pairs with the transverse pair momentum between 0-0.4 (GeV/c) the presented parametrization deviates from this point. This uncertainty was included in the systematic error of the measurement for this point. The straight line fit to the points

$$\mathcal{A} = P0 \cdot \exp(P1 \cdot \Delta R) \tag{7.6}$$

was used to convert the $\mathcal{A}$ parameter for a given $P_\perp$ bin to the pion-proton displacement. The systematic error is calculated assuming no correlations between the two fit parameters. The resulting of displacements are compared to a Blast-Wave model and to hydrodynamical calculations in Sections 8.3.

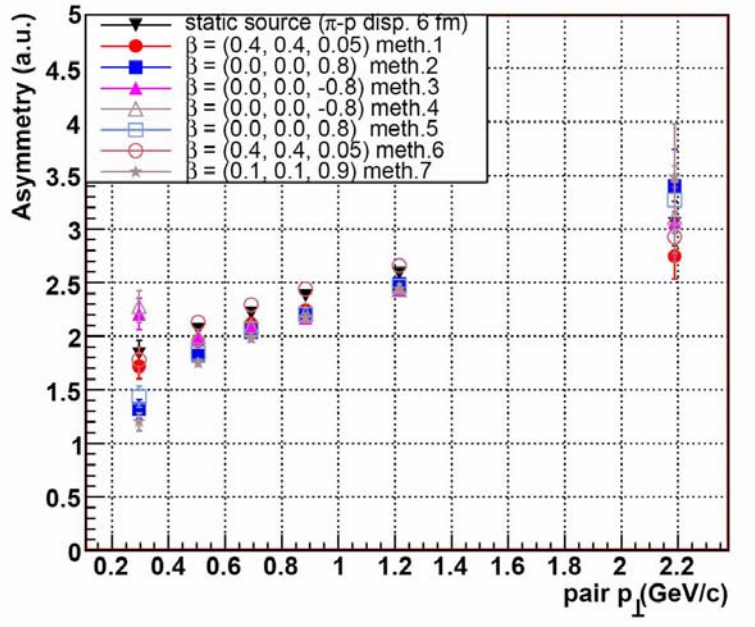

Figure 7.10: The asymmetry parameter deviation for different models of particle source emission.

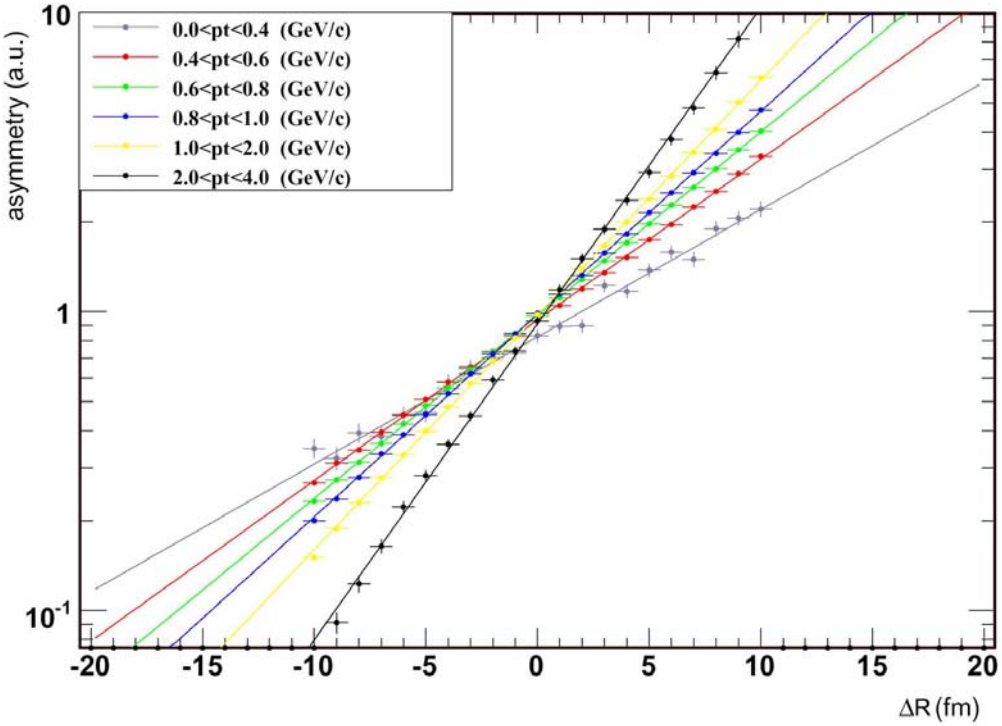

Figure 7.11: The asymmetry-to-displacement calibration.

Chapter 8

Discussion of the Results

In this chapter the results of the two-particle correlation analysis are discussed in the framework of a hydrodynamical model and the blast-wave parameterization. The Bose-Einstein correlations at a beam energy of 158 AGeV were analyzed as a function of centrality and in bins of pair rapidity and transverse momentum, as well as the azimuthal angle with respect to the reaction plane. The obtained results support a collision picture with longitudinal and transverse expansion. The individual dependences are discussed in detail below.

8.1 Transverse Momentum and Centrality Dependence of the HBT Radii

The space-time variances $\langle \tilde{x}_\mu \tilde{x}_\nu \rangle(\mathbf{P})$ depend on the pair momentum P. To understand their physical meaning, one can consider an observer who views a strongly expanding collision region. Some parts of the collision region move towards the observer and the particle spectrum emitted from those parts will appear blue-shifted. Other parts move away from the observer and appear red-shifted. Thus, if the observer looks at the collision system with a wavelength filter of some frequency, he sees only part of the collision region. Adopting a notion coined by Sinyukov, the observer sees a "region of homogeneity". In HBT interferometry, the wavelength filter is the pair momentum **P**. The direction of the pair momentum vector corresponds to the direction from which the collision region is viewed, thus inspecting different collision regions. In the Gaussian approximation, the region of the homogeneity is described by a four-dimensional space-time ellipsoid centered around $\langle \tilde{x}_\mu \rangle(\mathbf{P})$ and characterized by the emission function $S(\mathsf{x}, \mathsf{P})$ (see Eq. 1.30). The widths of this regions of homogeneity correspond to the space-time variances $\langle \tilde{x}_\mu \tilde{x}_\nu \rangle(\mathbf{P})$, see Eq. 1.35. Thus, HBT radius parameters give access to the space-time variances $\langle \tilde{x}_\mu \tilde{x}_\nu \rangle(\mathbf{P})$ but they do not depend on the effective source center $\langle \tilde{x}_\mu \rangle$. In the terms of space-time variance with the infinitely long source with boost-invariant longitu-

dinal expansion Makhlin and Sinyukov [MS88] provided a connection between the measured HBT radii and the geometry of the collision region. In this model the R_{long} radii is determined by the inverse of the longitudinal velocity gradient meaning that it rather describes the longitudinal length of homogeneity in the source than the geometrical size. Expanding the exponent of the emission function $S(\mathsf{x}, \mathsf{P})$ presented in [WH99] (Eq.5.1) around $x_{\mu=0}$ and using the saddle point approximation one can parameterizes the transverse dynamical length of homogeneity by

$$\begin{aligned} R^2_{out}(P_\perp) &= R^2_{side}(P_\perp) + \frac{1}{2}\left(\frac{T}{M_\perp}\right)^2 \beta^2_\perp \tau^2_0 \ , \\ R^2_{side}(P_\perp) &= \frac{R^2_{GEOM}}{1+\frac{M_\perp}{T}\eta^2_f} \ , \end{aligned} \tag{8.1}$$

where T is the freeze-out temperature, $M_\perp = \sqrt{m^2_\pi + (P_\perp/2)^2}$, $\beta_\perp$ is the mean transverse flow, η_f is the transverse flow rapidity of the source, and R_{GEOM} characterized the geometrical transverse size of the fireball freeze-out. This simple expressions illustrate several of the key concepts employed in HBT interferometry, namely, the overall size of the transverse radius parameters is determined by the transverse Gaussian widths of the collision region, and the difference $R^2_{out} - R^2_{side}$ is proportionally to the emission duration $\beta^2_\perp \left\langle \tilde{t}^2 \right\rangle$. Moreover, the transverse radii are sensitive to the transverse flow rapidity of the source which imply that the HBT radius shrinks for finite η_f since a dynamically expanding source viewed through a filter of wavelength **P** is seen only partial. This shrinking effect increases for larger values of the pair transverse momentum proportionally to the the ratio $\frac{\eta^2_f}{T}$. The $P_\perp$ dependence of the R_{side} is a consequence of transverse position-momentum correlations in the source with here originate from the transverse collective flow. Moreover, for the scenario of a boost-invariant expansion in longitudinal direction, based on the saddle point approximation the R_{long} at rapidity $y = 0$ is given by [HB95]

$$R^2_{long} = \tau^2_f \frac{T}{M_\perp} \frac{K_2\left(\frac{M_\perp}{T}\right)}{K_1\left(\frac{M_\perp}{T}\right)} \ , \tag{8.2}$$

where τ_f the average freeze-out time, and K_1 and K_2 are the modified Bassel functions of order 1 and 2.

Before proceeding with studding the centrality and transverse momentum dependence, in Fig. 8.1 we compare the radii obtained for central collisions (0-5% of σ_{GEOM}) with those previously published [A$^+$03a]. Slight discrepancies visible at the lower and the highest $P_\perp$ can be attributed to the improved understanding of the Coulomb influence on the measured correlation functions and the two-track resolution, respectively.

The complete $P_\perp$-dependence of the identical-pion HBT radii for seven classes of centrality and Y range of (1.3-2.8) is shown in Figs.8.1-8.2.

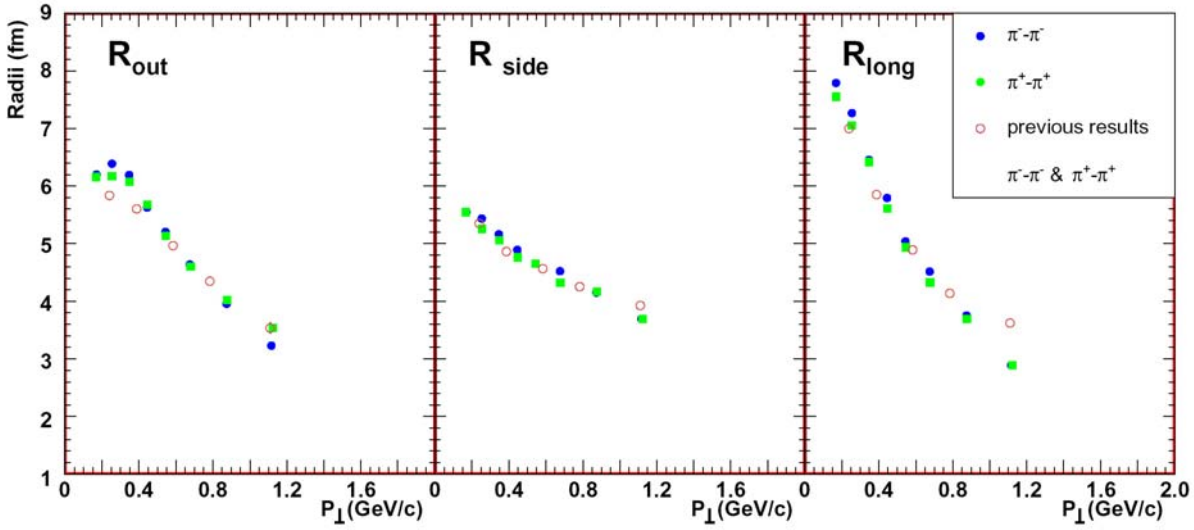

Figure 8.1: Previously obtained HBT radii for the most central events (<5 % $\sigma/\sigma_{\mathrm{GEOM}}$) [A^{+}03a] together with the results presented in this work. Both results were corrected for the Coulomb interaction and the detector resolution.

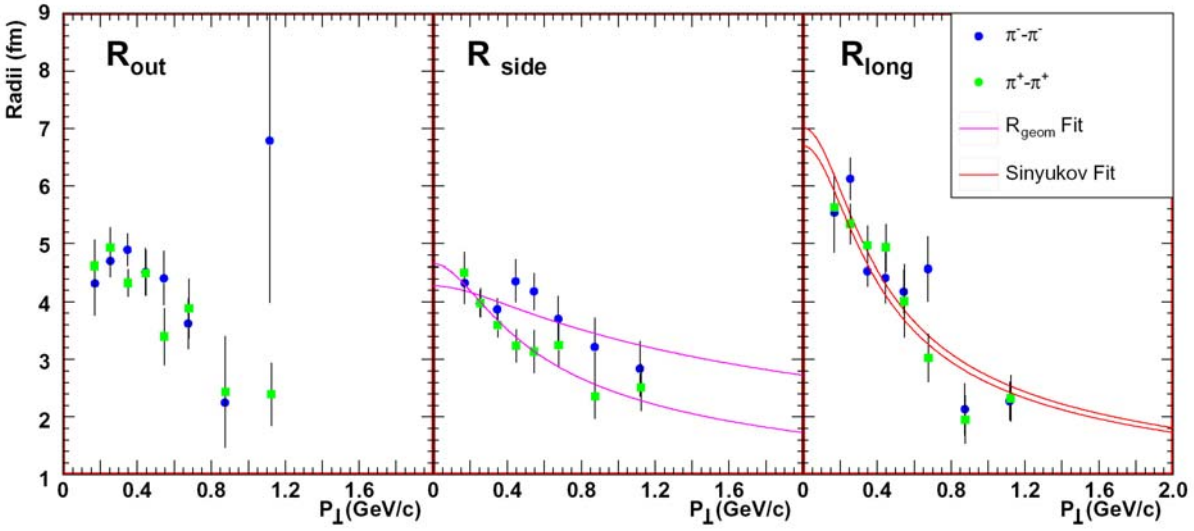

Figure 8.2: Transverse momentum dependence of the HBT radii corrected for the Coulomb interaction and detector resolution for centrality bin 25-35 %.

The R_{side} and R_{long} are fitted with Eq. 8.1 and Eq. 8.2. The results obtained from the hydro-inspired parameterization of the source expansion in the case of the R_{long} confirm the results of the previous CERES HBT analysis. The parameters derived from the fit of the Eq. 8.1 are

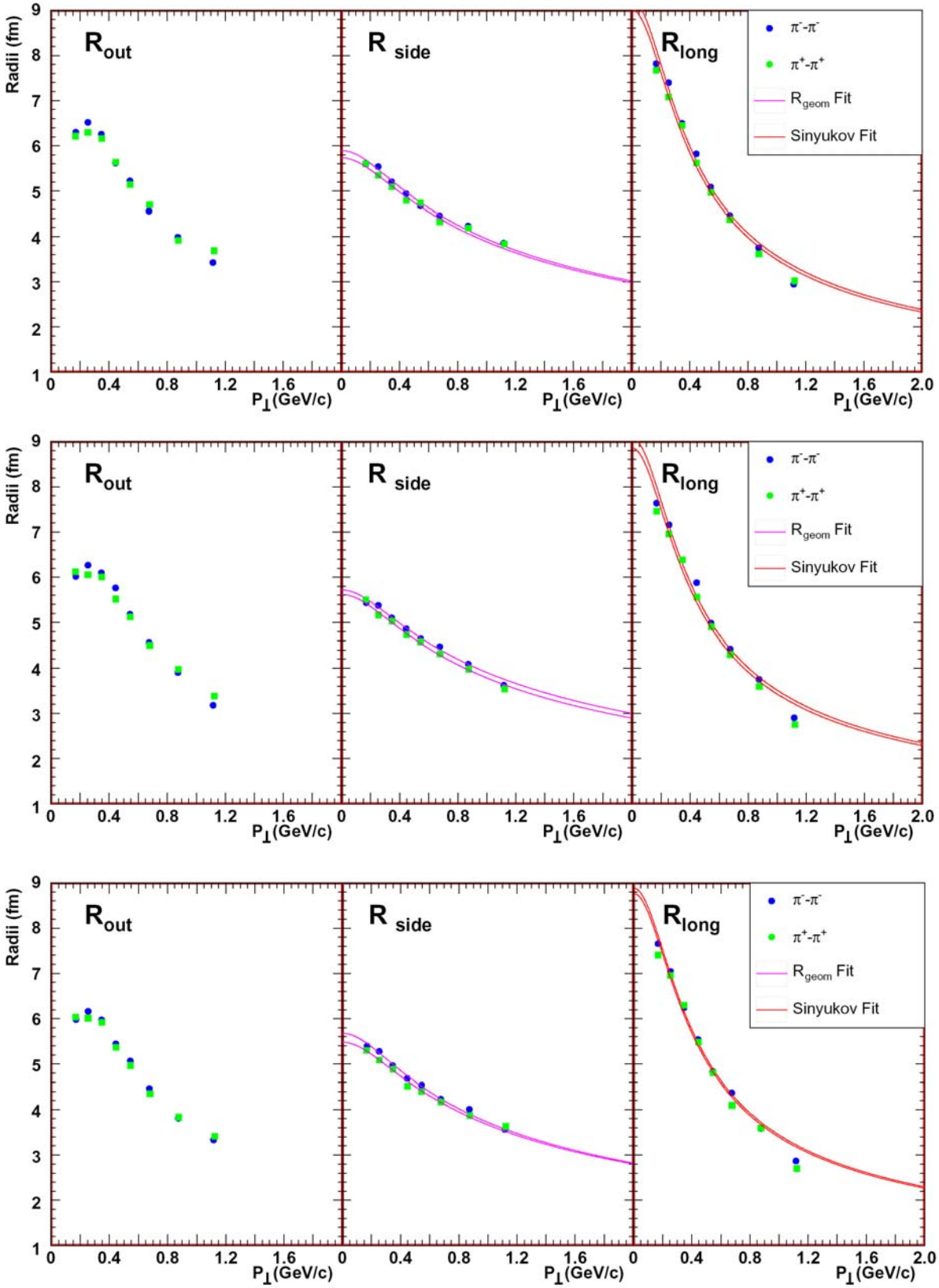

Figure 8.3: Transverse momentum dependence of the HBT radii corrected for the Coulomb interaction and the detector resolution. The top, the middle, and the bottom panel show the radii obtained for the centrality of 0-2.5 %, 2.5-5 %, and 5-7.5 %, respectively.

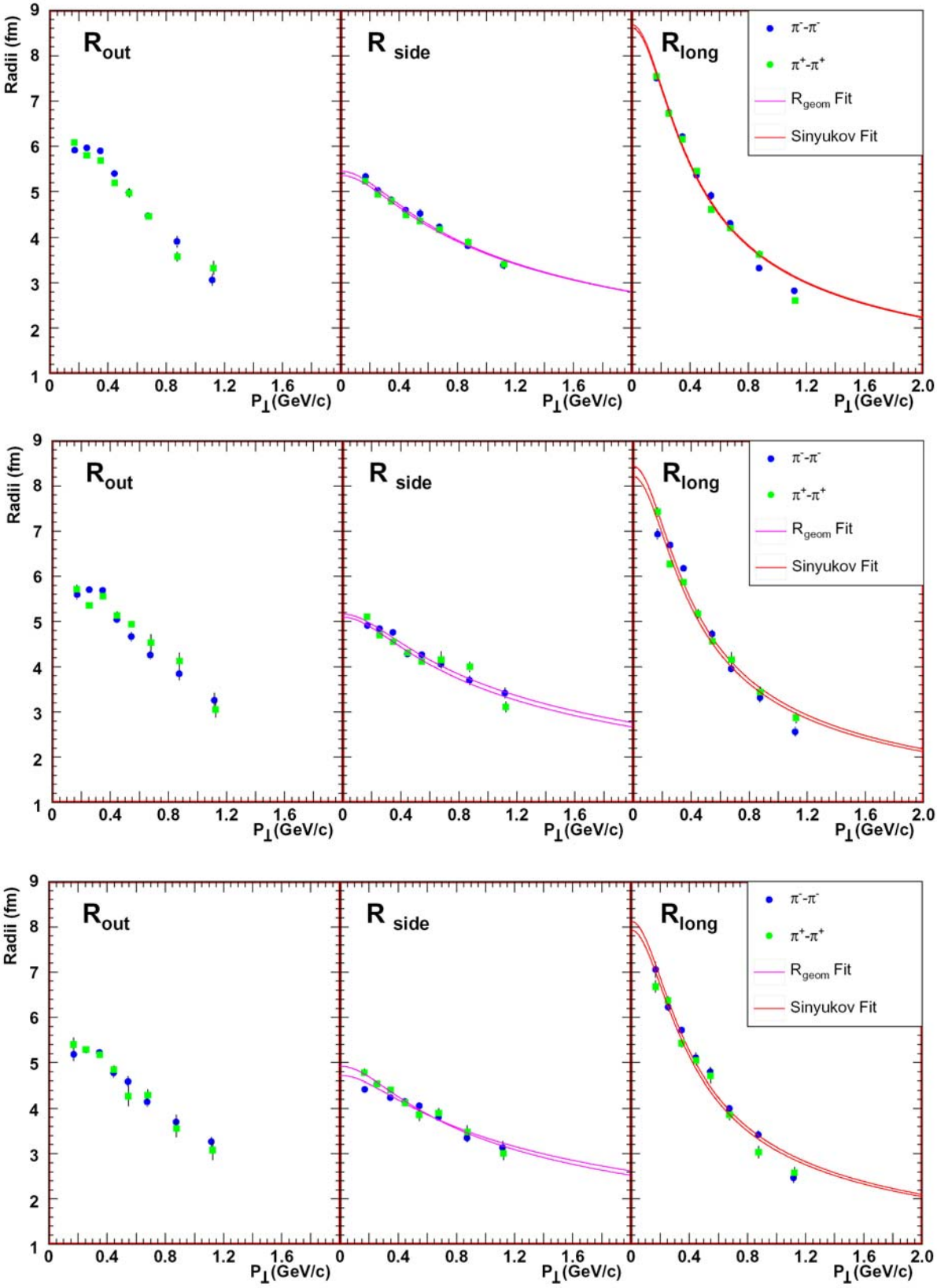

Figure 8.4: Transverse momentum dependence of the HBT radii corrected for the Coulomb interaction and the detector resolution. The top, the middle, and the bottom panel show the radii obtained for the centrality of 7.5-10 %, 10-15 %, and 15-25 %, respectively.

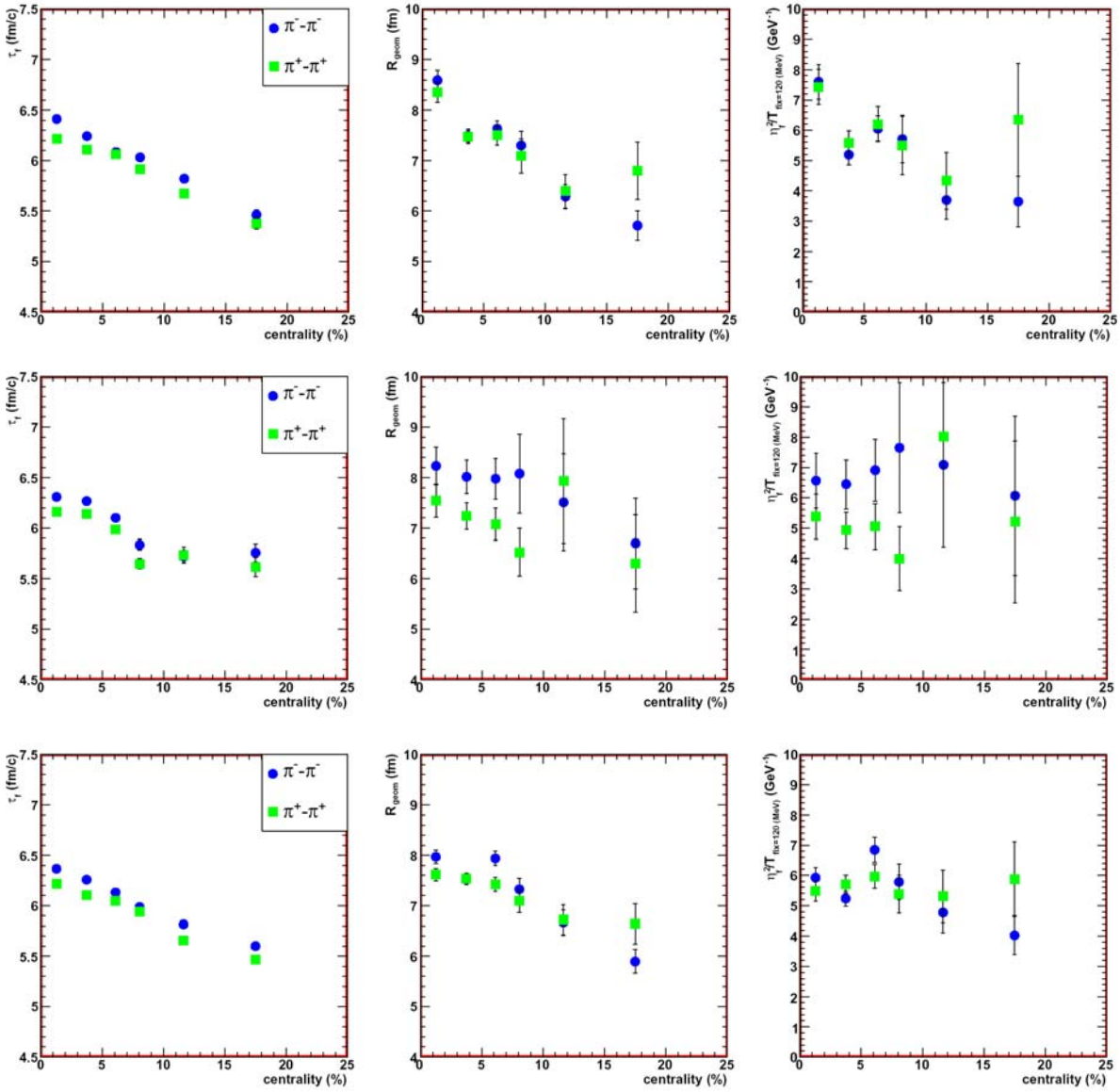

Figure 8.5: The extracted parameters of the emitting source based on the hydrodynamical scenario for three rapidity intervals. All results were obtained for a fixed freeze-out temperature of 120 MeV. Top panel: Y= 1.3-2.3. Middle panel: Y=2.3-2.8. Bottom panel: Y=1.3-2.8.

slightly above previous results, however, this can be attributed to the different rapidity selection used in both analysis. The results of the fits are compiled in Fig. 8.5.

8.2 Azimuthally Sensitive HBT Analysis

The dependence of the HBT radius on the azimuthal orientation with respect to the reaction plane $\Phi = \phi_{pair} - \Psi_2$ was fitted by [HHLW02]

$$\begin{aligned}
R^2_{out}(P_\perp, \Phi) &= R^2_{out,0}(P_\perp) + 2R^2_{out,2}(P_\perp)\cos(2\Phi) \\
R^2_{side}(P_\perp, \Phi) &= R^2_{side,0}(P_\perp) + 2R^2_{side,2}(P_\perp)\cos(2\Phi) \\
R^2_{long}(P_\perp, \Phi) &= R^2_{long,0}(P_\perp) + 2R^2_{long,2}(P_\perp)\cos(2\Phi) \\
R^2_{out-side}(P_\perp, \Phi) &= R^2_{out-side,0}(P_\perp) + 2R^2_{out-side,2}(P_\perp)\sin(2\Phi) \\
R^2_{out-long}(P_\perp, \Phi) &= R^2_{out-long,0}(P_\perp) + 2R^2_{out-long,2}(P_\perp)\sin(2\Phi) \\
R^2_{side-long}(P_\perp, \Phi) &= R^2_{side-long,0}(P_\perp) + 2R^2_{side-long,2}(P_\perp)\sin(2\Phi)\ . \qquad (8.3)
\end{aligned}$$

The 0^{th}-order Fourier coefficient coincides with the HBT radii from an azimuthally-integrated analysis while the 2^{nd}-order Fourier coefficient corresponds to the magnitude of the emission source asymmetry. In Fig. 8.6 the normalized 2^{nd}-order Fourier coefficients are shown as a function of centrality.

If the pion source were to reflect the initial collision geometry (almond shape out-of-plane) a positive $R_{side,2}$ and a negative $R_{out,2}$ should be expected. While $R_{out,2}$ seems to be negative indeed, $R_{side,2}$ is consistent with zero (Fig. 8.6). $R_{long,2}$, for which in first order no effect is expected, behaves similarly to $R_{out,2}$. Systematic checks revealed that the 2^{nd}-order Fourier coefficients are strongly affected by details of the event mixing procedure, particularly by the requirement that the two events should have a similar orientation of the reaction plane. This requirement controls small oscillations in the flat parts of the correlation function, visible in the two-dimensional projections of the correlation functions (Fig. 8.7), and possibly via them the second Fourier component of the correlation radii. Performing the event mixing in bins of 15° rather then 45° makes the small oscillation less dependent on the orientation with respect to the reaction plane and brings the second Fourier component of the R_{out} and R_{side} closer to zero (square in Fig. 8.6) With this, the observed pion source seems to be round in the transverse plane within the measurement errors. This is surprising because both at lower [Col00] and higher [Col04] beam energies asymmetric sources were observed. In Fig. 8.8 the results of the normalize 2^{nd}-order Fourier coefficients derived for different beam energies is shown.

8.3 Pion-Proton Source Displacement

The measured asymmetry of the correlation functions for pion-proton, discussed in Section 6, indicate that the pions and protons are not emitted from the same average space-time point. The unlike-sign pion correlations, on the other hand, do not shown significant asymmetry. This

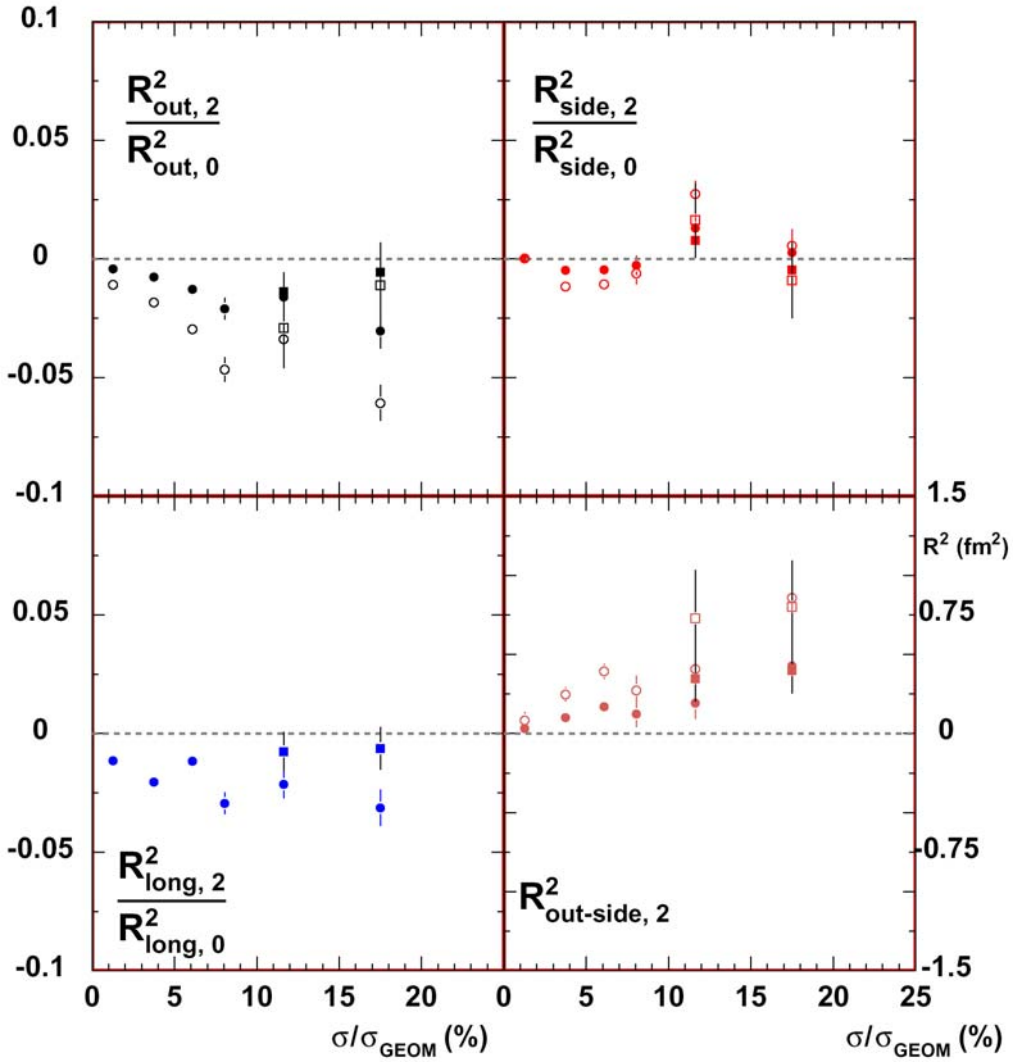

Figure 8.6: Fourier coefficient of azimuthal oscillations of HBT radii as a function of the event centrality for π^+ and π^- pairs combination (0.0-2.0 GeV/c). The close (open) symbols correspond to the uncorrected (corrected) 2^{th}-order Fourier coefficient for influence on finite reaction plane resolution. The squared symbols correspond to the results obtained with the different approach of the event mixing background construction (see text).

indicates that the effect is related to the particle mass. The parameterization presented in Section 7.4 was used to convert the measured asymmetry $\mathcal{A}$ of the correlation functions to the spatial separation between the particles at freeze-out. The conversion was performed assuming similar emitting source size as well as the finite momentum resolution. The assumption of the emission source sitting at midrapidity was included in the systematic error of the measurement.

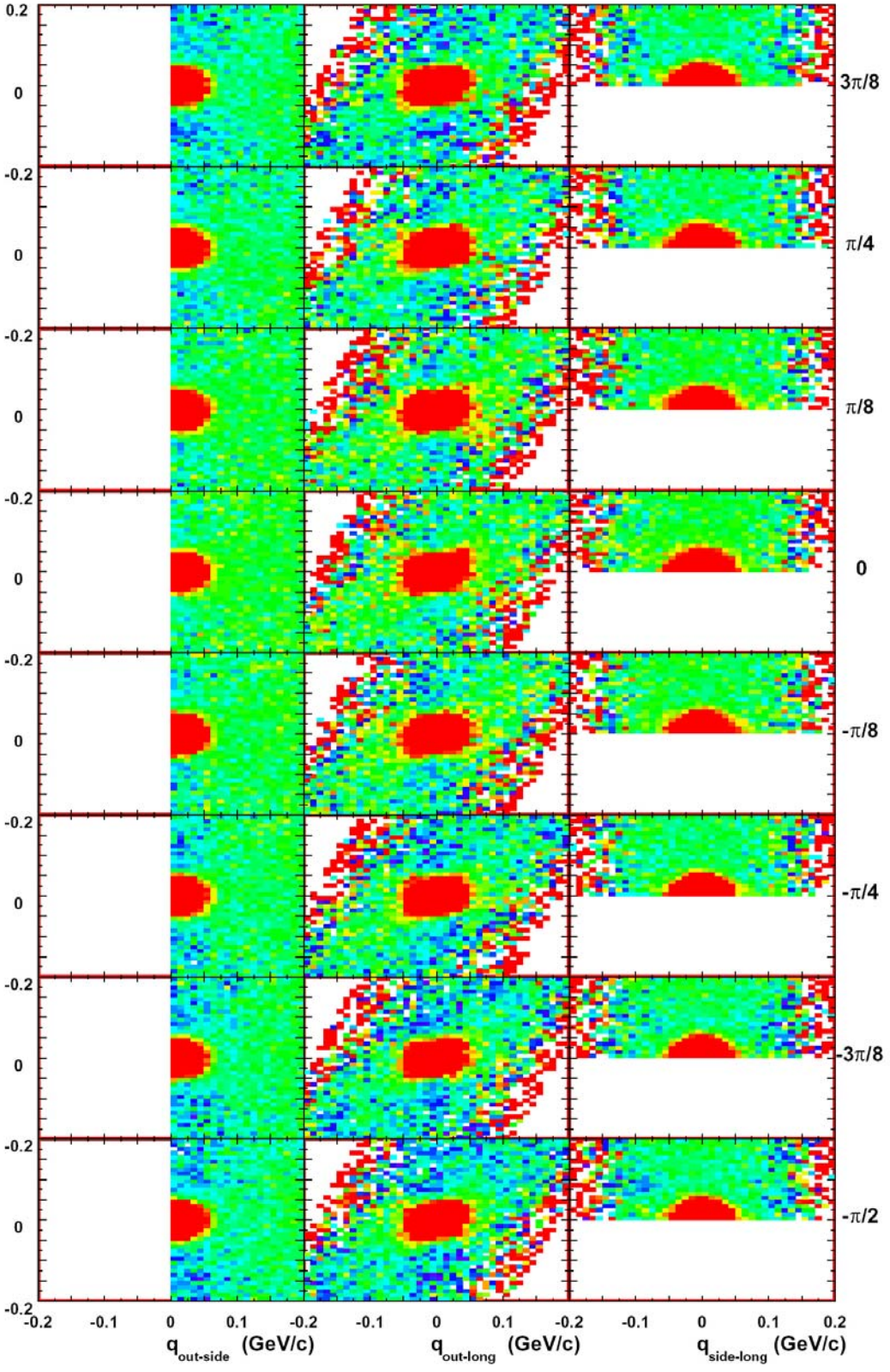

Figure 8.7: The two-dimensional HBT correlation functions as a function of the $\phi_{pair} - \Psi_2$ angle. The z-axis is set to be constant for all bins of $\phi_{pair} - \Psi_2$ ($0.985 \geq z \geq 1.035$).

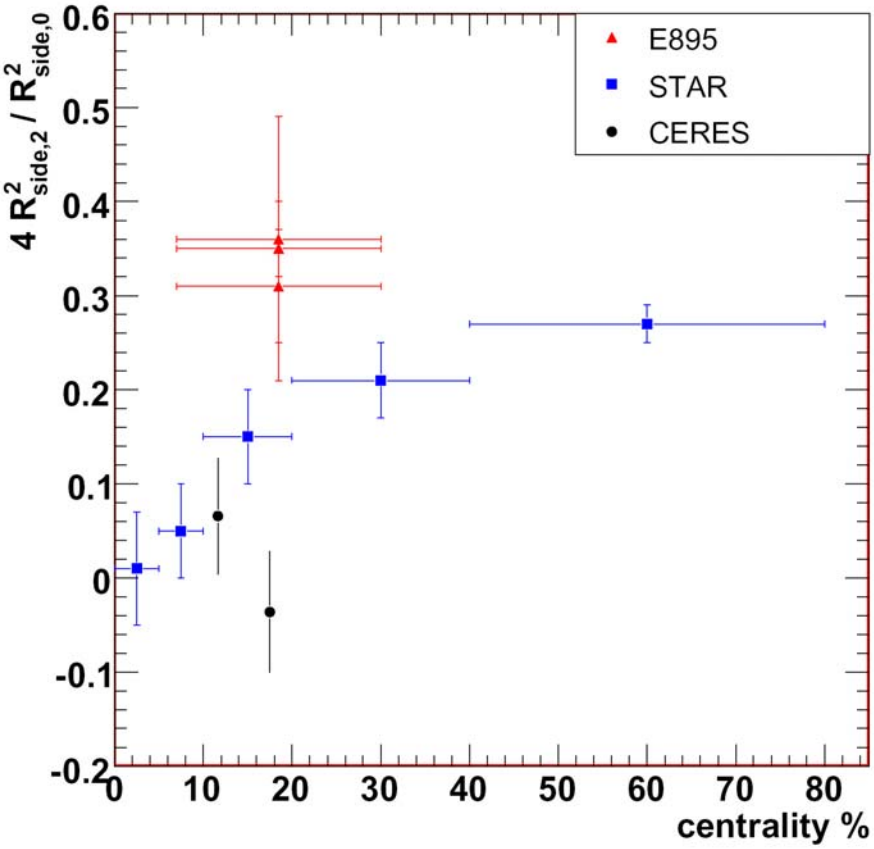

Figure 8.8: The centrality dependence of the source anisotropy measured for different beam energies.

In Fig. 8.9 the source displacement as a function of the pair transverse momentum for three different pair combinations are shown. The similarity between the π^+p and π^-p results indicates that the Coulomb interaction with the positive charged fireball is negligible, consistent with the fact that the spectra of the corresponding particles are in good agreement [AftSC04].

The asymmetry between pion-proton space-time emission, generated by the UrQMD model [BZS$^+$99] which produces radial flow through hadronic rescattering, is shown in Fig. 8.9 as green curves. The model predicts the dominance of the spatial part of the asymmetry generated by large transverse flow. Thus, the pion-proton separations were calculated assuming only the displacement in out direction. The results of such calculation are in agreement within the results obtained for asymmetry measured by experiment.

The observed increase of $\mathcal{A}$ with the pair transverse momentum ($\beta_\perp = P_\perp/M_\perp$), starting from zero due to symmetry reasons, can be parameterized as proposed by Lendnický and Sinyukov in [Led04, SVA96]. Assuming the longitudinal-boost invariance, a linear non-

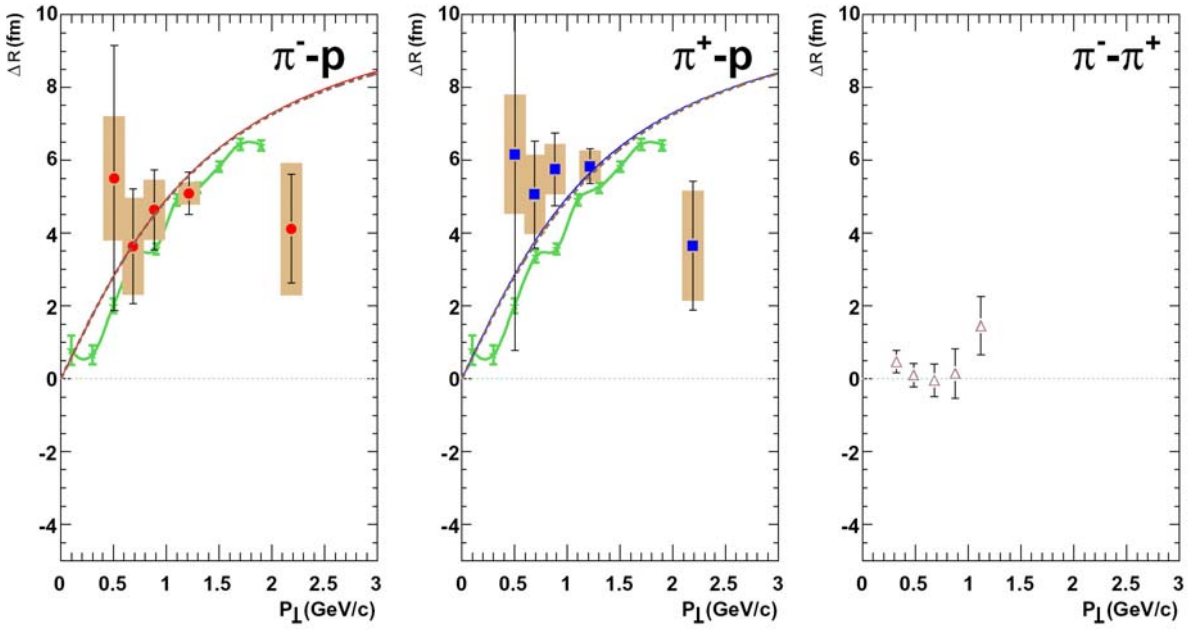

Figure 8.9: The source displacement ΔR as a function of the pair transverse momentum. The full symbols correspond to asymmetry obtained from the π^+-p$^+$ (square) and from the π^--p$^+$ (circle) correlation functions, respectively. The obtained results of the source displacement between (π-p$^+$) from the UrQMD (ver.1.3) are shown as a solid curve (green). The open triangles represent results derived for the unlike pion correlation functions. Fit to the data is based on Eq. 8.4 (see text).

relativistic transversal flow profile $\beta_F = \beta_0 \frac{r_\perp}{R_{GEOM}}$, the local thermal momentum distribution characterized by the kinetic freeze-out temperature T and Gaussian density profile $\exp\left(-r_\perp^2/(2R_{GEOM}^2)\right)$, one expects a rise of ΔR with the transverse pair velocity

$$\Delta R = \frac{R_{GEOM}\,\beta_\perp\,\beta_0}{\beta_0^2 + T/M_\perp}\,. \tag{8.4}$$

The mean transverse velocity is defined as

$$\beta_\perp = \frac{1}{\sqrt{1 + \left(\frac{m_\pi + m_p}{P_\perp}\right)}}\,, \tag{8.5}$$

and $M_\perp$ is the pair transverse mass, defined as

$$M_\perp = \sqrt{\sqrt{m_\pi^2 + \frac{m_\pi}{m_p + m_\pi}\cdot\left(\frac{P_\perp}{2}\right)^2}\cdot\sqrt{m_p^2 + \frac{m_p}{m_\pi + m_p}\cdot\left(\frac{P_\perp}{2}\right)^2}}\,, \tag{8.6}$$

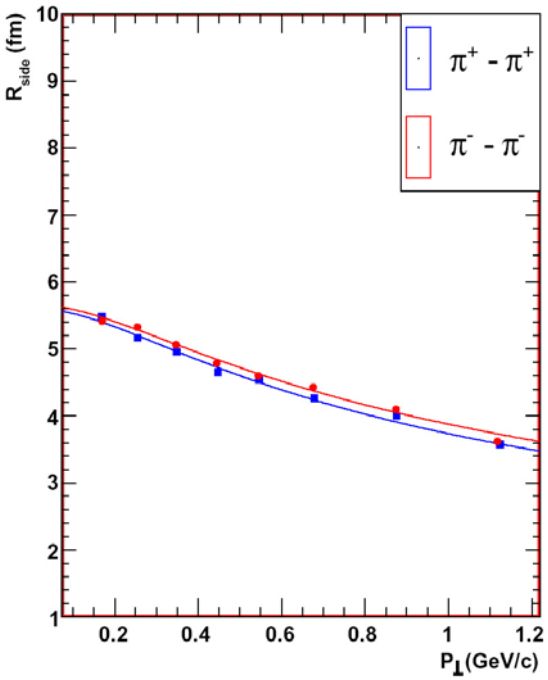

Figure 8.10: The R_{side} fitted by Eq. 8.4 together with ΔR. Presented radii were integrated over the centrality range (0-25%) and the HBT radii were derive.

where m_π and m_p are mass of pion and proton, respectively.

The derived ΔR $P_\perp$-dependence of the same- and the opposite-sign pion-proton pair correlations were fitted by Eq. 8.4 and the results are shown as the red and blue curves, respectively. Simultaneously the $P_\perp$-dependence of the HBT radius, R_{side}, derived from the two-particle correlations analysis for $\pi^+\pi^+$ and $\pi^-\pi^-$, were fitted with Eq.8.1 (see Fig 8.3). Assuming a common kinetics freeze-out temperature T, geometric transverse size of the fireball at the freeze-out R_{GEOM} and the transverse flow rapidity η_f

$$\eta_f = \frac{1}{2}\log\frac{1+\beta_0}{1-\beta_0} \tag{8.7}$$

it is possible to extract from both measurements all common parameters. The transverse collective flow which causes the $P_\perp$-dependence of R_{side} is at this same time responsible for the different space-time emission of various particle species. The dash brown curve in Fig. 8.9 represents the simultaneous fit to the all four results (asymmetry and R_{side} dependences) and results in the common fit parameters for both charges. In Table 8.1 the collection of the fit parameter derived from presented parameterization are gather. In Fig. 8.11 the contours of χ^2 as a function of the fit parameters R_{GEOM}, β_0, and T are shown. It is worthy of notice that depending on the charge combination of the two-particles correlations the slightly different fit values are preferred.

The results of the hydro-inspired blast wave parameterization are presented in the next section.

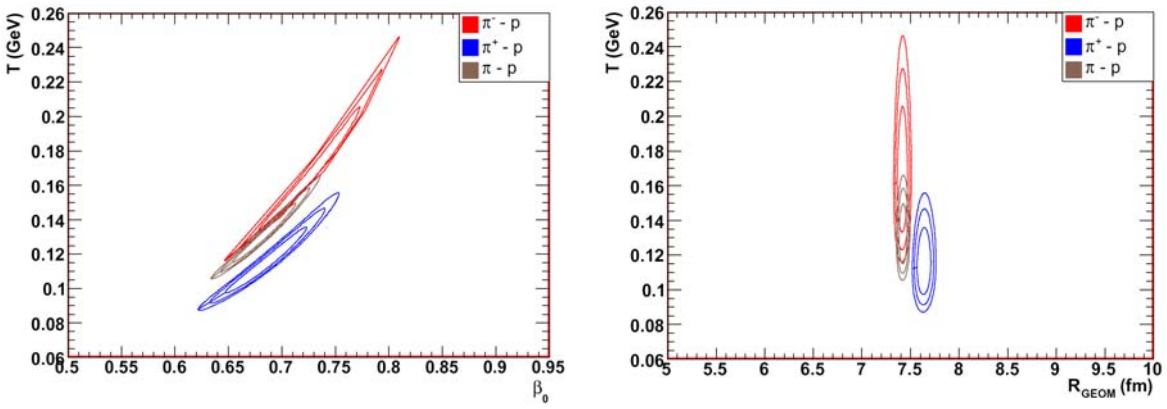

Figure 8.11: The 1-3σ contours plots of χ^2, obtained by simultaneous fit of Eq. 8.4 to ΔR and R_{side}.

Fit par.	$\pi^+ - p$	stat. err.	$\pi^- - p$	stat. err.	$\pi - p$	stat. err.
β_0	0.695	0.007	0.655	0.006	0.663	0.004
$R_{GEOM}(fm)$	7.638	0.07	7.412	0.052	7.421	0.04

Table 8.1: The collection of fit results obtained for T_f = 120 MeV.

8.4 Hydrodynamics and Blast Wave Model Parameterization

The hydrodynamical models will describe the evolution of a collision system only when the time scales of the microscopic processes within the system are significantly smaller than the time scale of the macroscopic evolution of the system. In heavy ion collisions this implies that the average time between two successive interactions between partons is much smaller than the life time of the system, and leads to the termalization of the system. Once the system is in equilibrium the hydrodynamical formalism can be applied.

In this section the CERES results obtained from the hadrons analysis in the top central 7% are presented together with the hydrodynamical calculations performed by P. Huovinen [KHHH01]. The calculations were performed in 2+1 dimensions assuming a boost-invariant longitudinal flow. The initial conditions were fixed via a fit to the $p_\perp$ spectra of negatively charged particles and protons in Pb+Pb collisions at the top SPS energy [KSH99]. The equation of state which is an integral part of hydrodynamical calculations assumed the 1-st order phase transition to the QGP at the critical temperature of T_c = 165 MeV. The presented calculations were obtained for the freeze-out temperature of 120 MeV. In Fig. 8.4 the single transverse momentum spectra of all negative hadrons for two bins of rapidity ($Y_1 = \langle 2.1 \rangle$ (black points), $Y_2 = \langle 2.6 \rangle$ (blue points)) and of neutral kaons are shown together with the hydrodynamical calculations (red

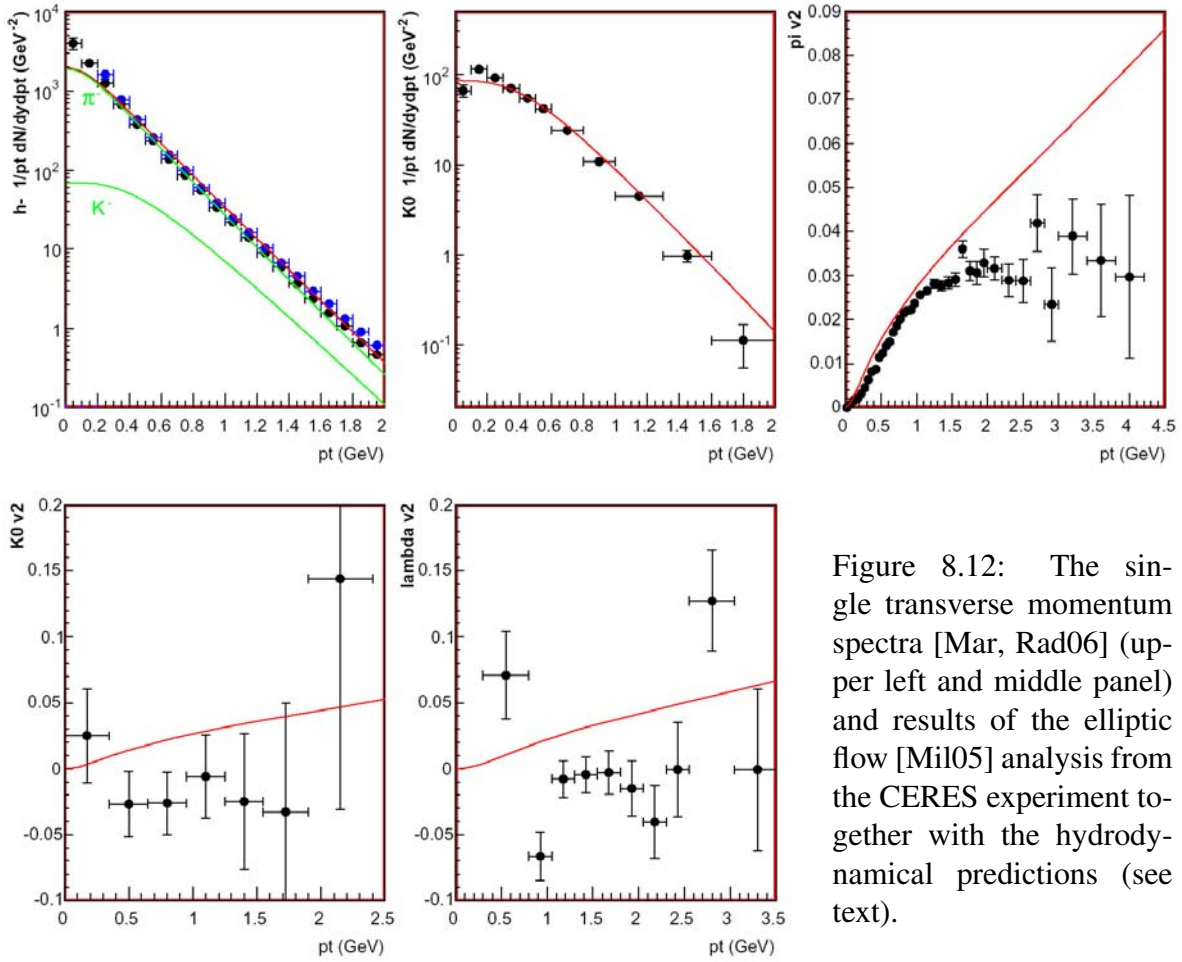

Figure 8.12: The single transverse momentum spectra [Mar, Rad06] (upper left and middle panel) and results of the elliptic flow [Mil05] analysis from the CERES experiment together with the hydrodynamical predictions (see text).

curves). The elliptic flow of charged pions, neutral kaons, and hyperons is presented as well. The comparison between the HBT radii and the hydrodynamical calculations of the source size based on the space-time variances are shown in Fig. 8.4. While the single particle transverse momentum spectra are rather well described the calculation fails in the case of two-particle correlations. The R_{side} parameter is underestimated and R_{out} and R_{long} are overestimated. This kind of discrepancy was observed for the first time at RHIC and for some time it was believed to be specific to this energy range.

The same data sets are reasonably well fitted by the blast wave parameterization [RL04]. In this particular version of the model longitudinal boost invariance is assumed. The azimuthal anisotropies are introduced via the geometrical ellipticity ($R_y > R_x$) and via the azimuthal dependence of the collective transverse rapidity $\rho(r,\phi) = r/R\rho_0 + \rho_2 * cos(2\phi)$. The fit parameters are

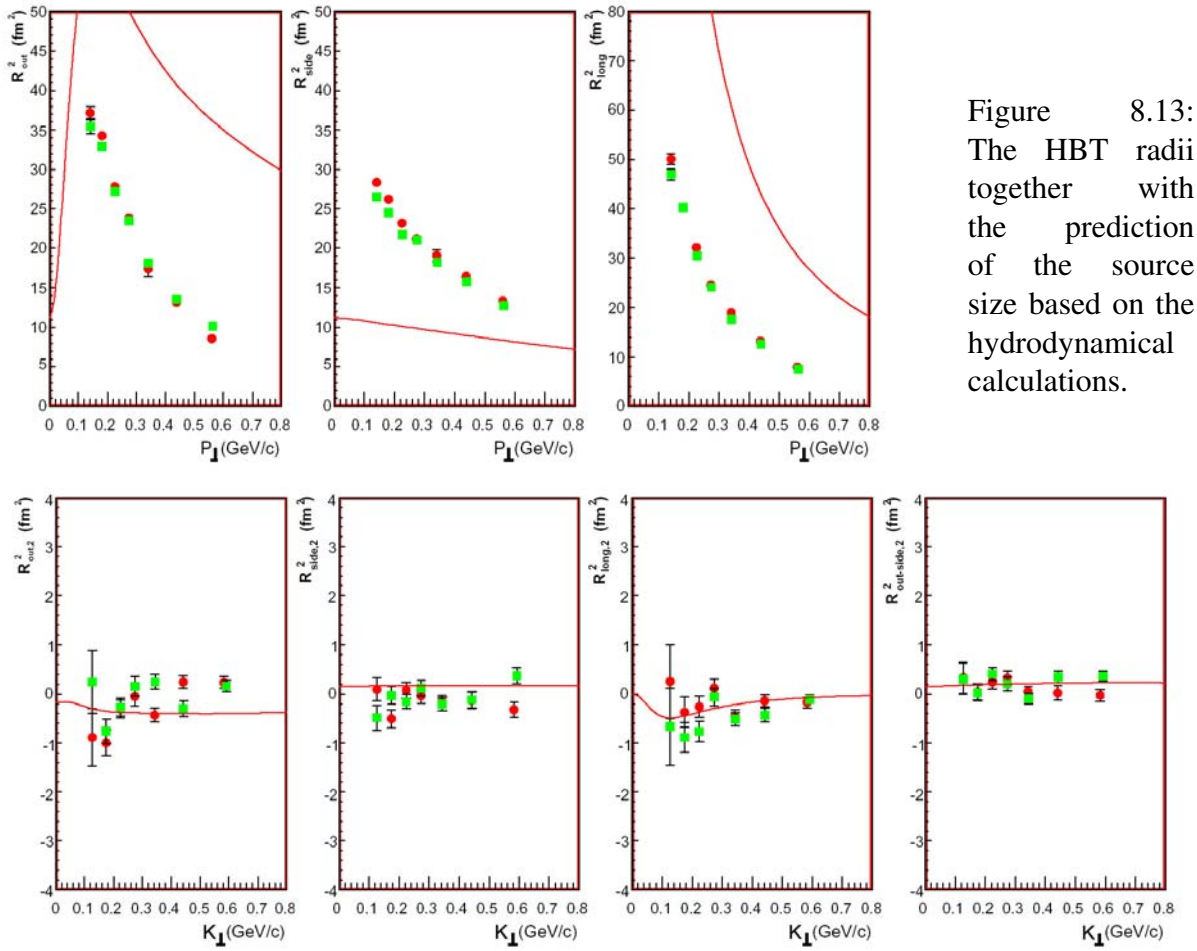

Figure 8.13: The HBT radii together with the prediction of the source size based on the hydrodynamical calculations.

- kinetic freeze-out temperature T,
- maximum flow rapidity ρ,
- source radii R_x and R_y,
- the system longitudinal proper time ($\tau = \sqrt{t^2 - z^2}$),
- the emission duration.

The blast wave fit was performed simultaneously to all the distributions, with a fixed freeze-out temperature $T = 100$ MeV and a sharp sphere profile (relative surface diffuseness of the emission source $a_s = 0.01$). In Table 8.2 the rapidity density of the particles are shown.

$pi^{-}dN/dy$	152.7	pi^{-} multiplicity
$K^{0}dN/dy$	18.44	K^{0} multiplicity
$\phi dN/dy$	1.451	ϕ multiplicity
T	0.100 GeV	temperature (fixed)
ρ_0	0.87	mean transverse rapidity
ρ_2	0.016	second Fourier comp. of transv. rapidity
R_x	11.26 fm	source radius in-plane
R_y	11.42 fm	source radius out-of-plane
a_s	0.01	surface diffuseness (fixed)
τ_0	7.37 fm/c	freeze-out time
$d\tau$	1.55 fm/c	freeze-out duration

Table 8.2: The Blast-Wave fit results.

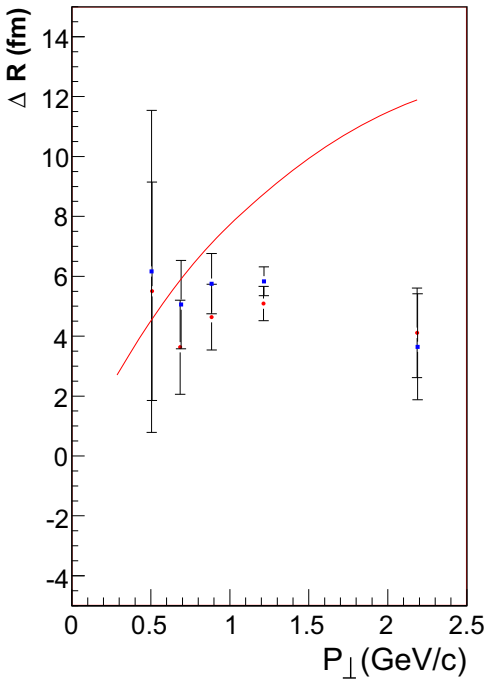

Figure 8.14: The Blast-Wave parameterization of pion-proton displacement.

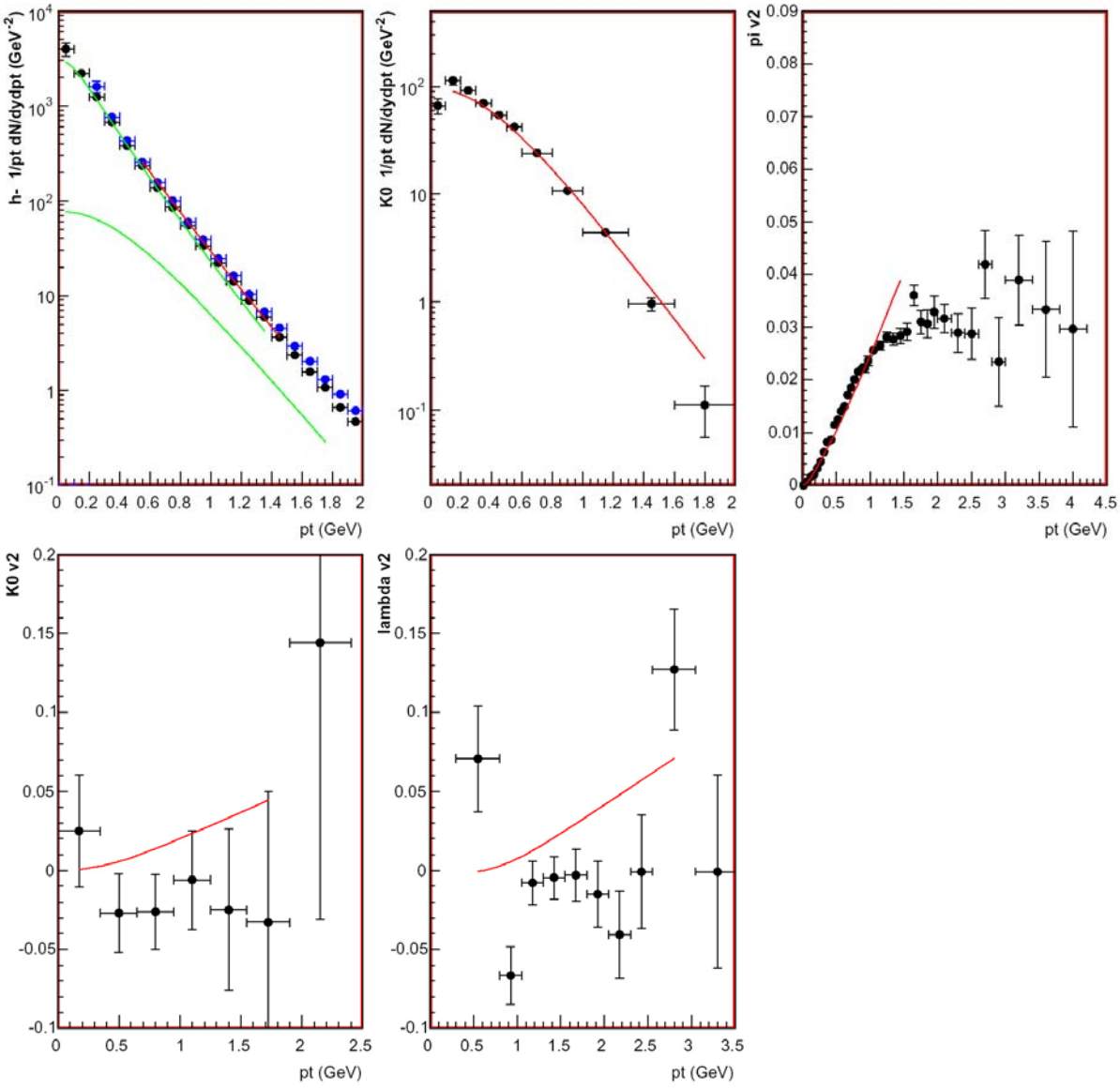

Figure 8.15: The Blast-Wave parameterization of flow and transverse spectra.

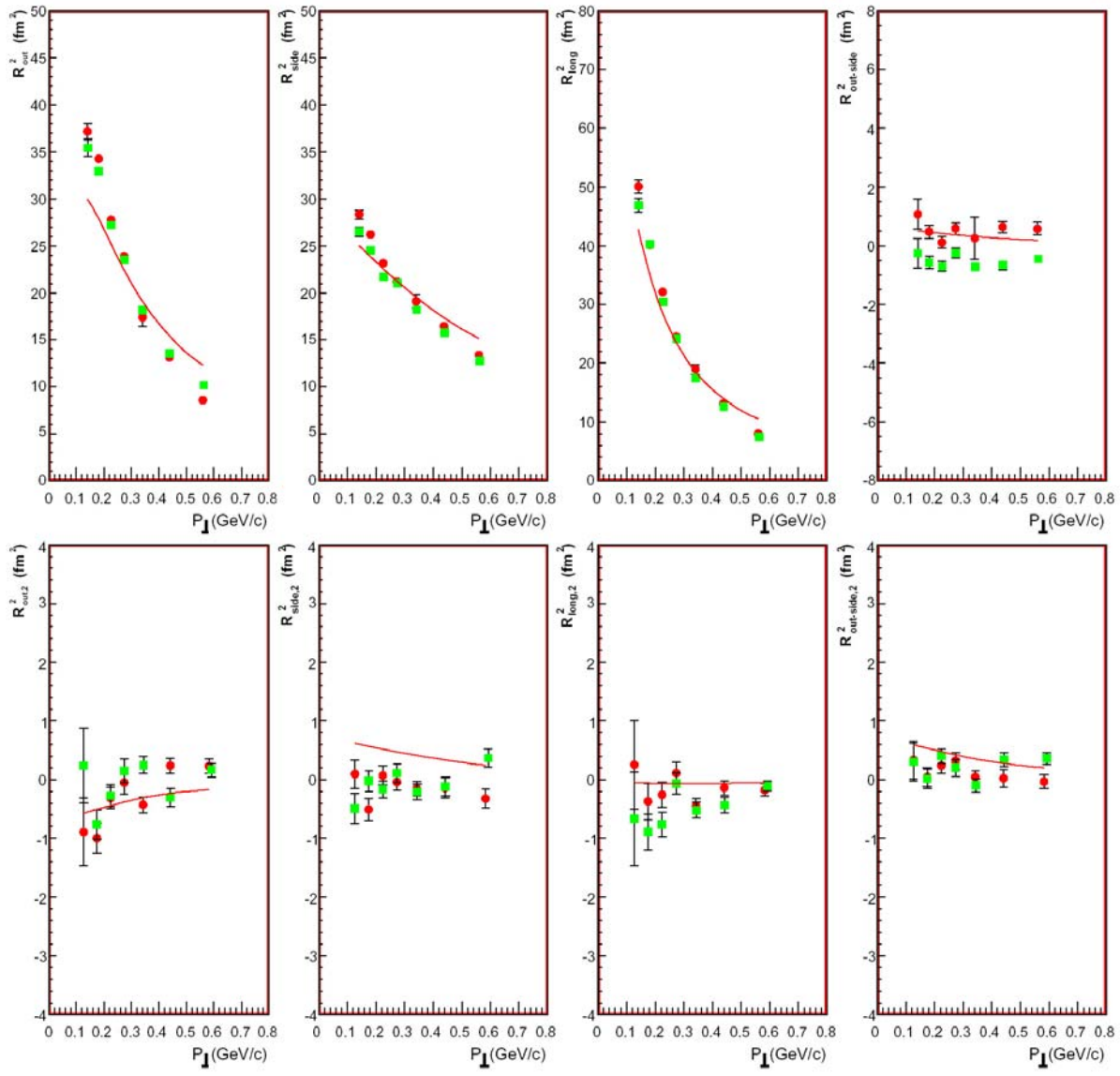

Figure 8.16: The Blast-Wave parameterization of HBT radii.

8.5 Summary

This thesis presents results of a two-particle correlation analysis applied to the central Pb+Au collision data at 158 GeV per nucleon, collected in the final run of the CERES experiment at the CERN SPS. The state-of-the art analysis of identical pion correlations yielded HBT radii which, in their centrality and transverse momentum dependence, are in good agreement with the previous preliminary analysis of a subset of the data and with the results of other experiments. The results support the collision picture with strong longitudinal and transverse expansion.

The high event statistics and the good understanding of the experiment's resolution and of the Coulomb correction allowed to employ two more sophisticated correlation techniques, the reaction plane dependent pion-pion HBT radius analysis and the pion-proton Coulomb correlation analysis. In the first one, the correlation radii were studied as a function of the pion azimuthal emission angle with respect to the reaction plane. The obtained pion source profile in the plane transverse to the beam direction is round within the experimental accuracy, in contrast to the results obtained in similar collision systems (albeit at lower centralities) at the AGS and at RHIC. In the pion-proton analysis, a finite displacement between the sources of pions and protons was derived from the asymmetry of the correlation peak in the pair momentum direction. With the help of a dedicated fast Monte Carlo simulation the displacement was estimated to be around 4-6 fm, with protons being emitted closer to the edge (or earlier) than pions. In a system with transverse expansion such a displacement arises naturally because of the collective transverse velocity added to the thermal velocity of particles with different masses. Since the maximum Coulomb interaction is for pairs in which the pion and the proton move at the same velocity, and since pions on average is much faster than protons, only relatively fast protons and relatively slow pions can contribute to the correlation peak. The fastest protons are the ones which freeze-out close to the edge of the fireball where the collective velocity kick is the highest; conversely, the slowest pions come from the center of the fireball.

The correlation radii obtained for identical pions and the source displacements deduced from the pion-proton correlations, along with the single transverse momentum spectra and the elliptic flow parameters, were compared to hydrodynamical calculations and to the blast wave model. The hydrodynamics significantly underestimates the R_{side} radius and overestimates R_{out} and R_{long}, similarly as it is the case at the RHIC energies. This indicates that this discrepancy might be caused by non-realistic predictions of the hydrodynamical approach rather than by some unusual reaction mechanism at RHIC, and that calling it "RHIC HBT puzzle" is therefore inappropriate. The blast wave model, on the other hand, fits the data rather well except for the somewhat overestimated second Fourier components of the HBT radii with respect to the reaction plane angle, pion-proton source displacement, and the detailed dependence of R_{side} and R_{out} on the transverse momentum. The latter might be possibly explained by the contribution of soft pions from decays of the short-lived resonances like Δ or ρ which through their finite $c\tau$ increase the effective source size.

Appendix A

step3c – Technical Information

The information, stored in the `step3c` ROOT tree format, was organized in two ROOT classes, the event (CSEvent) and the track (CSTrack). List of variables with short description for CSEvent and CSTrack classes are presented in tables A.1 and A.2 respectively. The information about non-vertex SDD tracks is stored in the CSTrack, and corresponding sets of variables, as for the SDD vertex tracks, are available by adding the suffix `_s` at the end of the SDD variable name. The access to all variables stored in the ROOT tree is provided by the associate member functions of the ROOT objects. After many calibrations of the `step3c` data set were performed, the collection of the member functions providing access to the fully tuned variables is also available e.g. the reaction plane angle Ψ_n, the centrality of the collision expressed in the percent of the geometrical cross section, the momentum, and the dE/dx of TPC track.

Table A.1: The list of variables stored in the CSEvent class.

variable type	variable name	description
Int_t	run	the run number
Int_t	burst	the burst number
Int_t	evt	the event number
Int_t	time	the production time of event
Int_t	pattern	the trigger pattern (beam=1, minb=2, cent=4, ...)
Int_t	rich1RecoveryTime	the time from last discharge Rich1 (20 ms)
Int_t	rich2RecoveryTime	the time from last discharge Rich2 (20 ms)
Float_t	beamBefore	the preceding beam in ns
Float_t	beamAfter	the following beam in ns
Float_t	BC1Adc	calibrated signal from BC1 beam detector

Continued on next page

Table A.1 – continued from previous page

variable type	variable name	description
Float_t	BC2Adc	calibrated signal from BC2 beam detector
Int_t	BC3Adc	by mistake this variable correspond to the multiplicity from MC
Float_t	centralityMC	the track multiplicity from MC
Float_t	centralitySD	the track multiplicity from SDD
Float_t	centralityTPC	the track multiplicity from TPC
Float_t	x1eta1SD	the Q_1^X from SDD, 1.7$< \eta <$2.2
Float_t	y1eta1SD	the Q_1^Y from SDD, 1.7$< \eta <$2.2
Float_t	x2eta1SD	the Q_2^X from SDD, 1.7$< \eta <$2.2
Float_t	y2eta1SD	the Q_2^Y from SDD, 1.7$< \eta <$2.2
Float_t	x1eta2SD	the Q_1^X from SDD, 2.2$< \eta <$2.7
Float_t	y1eta2SD	the Q_1^Y from SDD, 2.2$< \eta <$2.7
Float_t	x2eta2SD	the Q_2^X from SDD, 2.2$< \eta <$2.7
Float_t	y2eta2SD	the Q_2^Y from SDD, 2.2$< \eta <$2.7
Float_t	x1eta3SD	the Q_1^X from SDD, 2.7$< \eta <$3.2
Float_t	y1eta3SD	the Q_1^Y from SDD, 2.7$< \eta <$3.2
Float_t	x2eta3SD	the Q_2^X from SDD, 2.7$< \eta <$3.2
Float_t	y2eta3SD	the Q_2^Y from SDD, 2.7$< \eta <$3.2
Float_t	x1TPC	the Q_1^X from TPC
Float_t	y1TPC	the Q_1^Y from TPC
Float_t	x2TPC	the Q_2^X from TPC
Float_t	y2TPC	the Q_2^Y from TPC
Float_t	vertexX	the X position of the vertex in cm
Float_t	vertexY	the Y position of the vertex in cm
Float_t	vertexZ	the Z position of the vertex in cm
Int_t	ntracks	the TPC number of tracks
TClonesArray*	csTracks	the array of the CSTracks

Table A.2: The list of variables stored in the CSTrack class.

variable type	variable name	description
Char_t	SD_shared	the SDD hit shared by several SDD tracks, one can distinguish between no sharing case (=0) and sharing case (!=0)
Char_t	SD1_nanodes	the number of anodes

Continued on next page

Table A.2 – continued from previous page

variable type	variable name	description
Float_t	SD1_theta	the theta angle with respect to the event vertex
Float_t	SD1_phi	the phi angle with respect to the event vertex
Float_t	SD1_dedx	the dE/dx
Float_t	SD1_resum	the dE/dx resumed within 5 (mrad)
Float_t	SD1_dn	opening angle between closest-Hit and next closest-Hit
Char_t	SD2_nanodes	the number of anodes
Float_t	SD2_theta	the theta angle with respect to the event vertex
Float_t	SD2_phi	the phi angle with respect to the event vertex
Float_t	SD2_dedx	the dE/dx
Float_t	SD2_resum	the dE/dx resumed within 5 (mrad)
Float_t	RICH_phi	the phi of the ring
Float_t	RICH_theta	the theta of the ring
Float_t	RICH_radius	the ring radius
Float_t	RICH_nHits	the number of hits on ring for RICH1+2 corrected for background and acceptance
Int_t	RICH_nHits1_NC	the raw number of hits on ring in RICH1
Int_t	RICH_nHits2_NC	the raw number of hits on ring in RICH2
Float_t	RICH_sumAmp	the raw amplitude of hits on ring
Float_t	RICH_sigmaFit	the width of Gauss fit to distribution of hits vs. distance from predictor
Float_t	RICH_nHitsFit	area fit/binWidth
Float_t	RICH_COGshift	the displacement of COG of ring from predictor
Float_t	RICH_OLD_theta	the theta of the ring
Float_t	RICH_OLD_phi	the phi of the ring
Float_t	RICH_OLD_radius	the ring radius
Float_t	RICH_OLD_houghAmpl	the combined hough amplitude
Float_t	RICH1_OLD_sumAmpl	the sum of amplitude in the RICH1
Float_t	RICH2_OLD_sumAmpl	the sum of amplitude in the RICH2
Int_t	RICH_OLD_nHits	the number of hits in RICH1 and 1000*RICH2
Float_t	RICH_OLD_quality	the variance of the combined fit
Int_t	TPC_nHits	the number of fitted hits and 100*hits
Float_t	TPC_chi2rad	the fit quality, χ^2 in r vs. z

Continued on next page

Table A.2 – continued from previous page

variable type	variable name	description
Float_t	TPC_chi2phi	the fit quality, χ^2 in ϕ vs. z
Float_t	TPC_r0	the distance from the vertex in cm
Float_t	TPC_phi0	the phi angle between r0 and vertex in rad
Float_t	TPC_theta	the θ_{R2M} with respect to the event vertex
Float_t	TPC_phi	the ϕ_{R2M} with respect to event vertex
Float_t	TPC_thetaMean	the $< \theta >$ positions of all hits on a track
Float_t	TPC_phiMean	the $< \phi >$ positions of all hits on a track for 0-field and of the first four front hits in case on magnetic field
Float_t	TPC_dedx	the dE/dx
Float_t	TPC_pcor2	the momentum from 2-parameter fit
Float_t	TPC_pcor3	the momentum from 3-parameter fit

The source code and the calibration files were stored in the CERN Andrew File System (AFS). The main directories are listed in the table A.3. The _coolVersion correspond to the version of the COOL library used for production of step3c, and _UNITnr_ correspond to the unit number. First three directories correspond to the source code and production chain, and remaining folders contained necessary calibration and configuration files for CERES detector. The table A.4 shows the names of calibration files used for step3c production. The unit-by-unit dependent calibration and configuration files were located in ceres/prod/prod2000/calib/cal_UNITnr_/ called _calib_UbyU/. The calibration parameters of the vertex refitting procedure were stored for a given unit in the file vertexfit.dat, which was located in _calib_UbyU/ directory. The configuration files required by some COOL objects are listed in the table A.5.

Table A.3: The location of the directories used during production of the step3c.

directory name	location path
source	ceres/step3c/source
exec	ceres/step3c/exec
log_files	ceres/step3c/log_files
calib	ceres/sw/00/cool/_coolVersion/example/analyzer/calib/
config	ceres/sw/00/cool/_coolVersion/example/analyzer/config/ ceres/prod/prod2000/calib/cal_UNITnr_/
maps	ceres/sw/00/cool/_coolVersion/maps/

Table A.4: The default name of the calibration files was linked with the names described in the column used file. The filed column correspond to the configuration of the magnetic field in TPC.

field	default file	used file
pos	calib/tpc-dphiplmap-frompads.dat	maps/tpc-dphiplmap-pad-u_UNITnr_-cor.dat
neg	calib/dthemap.dat	calib/dthemap-bneg.dat
neg	calib/residuals_frompads_phi.dat	calib/residuals_bypads_bneg_ite0_ite1_phi.dat
neg	calib/residuals_frompads_r.dat	calib/residuals_bypads_bneg_ite0_ite1_r.dat
neg	calib/tpc-dtheplmap.dat	maps/tpc-dtheplmap-u_UNITnr_.dat

Table A.5: The configuration files of the given COOL object used during step3c production.

class name	configuration file
CTPCCalibrationSetup	calib_UbyU/setup.CTPCCalibration
CTPCLookupTable	calib_UbyU/tableBfield.bin
CTPC	config/setup.tpc calib_UbyU/setup.CTPCCalibration
CTPCTrackFitter	config/setup.tpctrackfitter config/track.ref
CSidc1	calib_UbyU/setup.sidc1 calib_UbyU/calibration.sidc1
CSidc1	calib_UbyU/setup.sidc2 calib_UbyU/calibration.sidc2
CRobustVertexFitter	config/setup.vertex
CPionTrackingStrategy	config/setup.pionstrategy

Appendix B

Non-identical Particle Correlation Functions

The non-identical correlation functions have been studied for $\pi^-\pi^+$, π^-p, and π^+p pair combinations. In Fig. B.1 derived projection of correlation functions for equal masses unlike-charge pair is shown. As expected, no significant asymmetry between left and right widths of the correlation functions is observed. The small inefficiency seen for pairs with the transverse momentum larger then 1 GeV/c is attributed to the remaining effects of the two-track resolution. However, as shown in Fig. B.2 and Fig. B.3 no such effects are observed in the case of non-identical particle correlations with different particles species used to construct the pair, as it was explained in chapter 6. The blue solid line is a fit of Eq. 6.2 to the data.

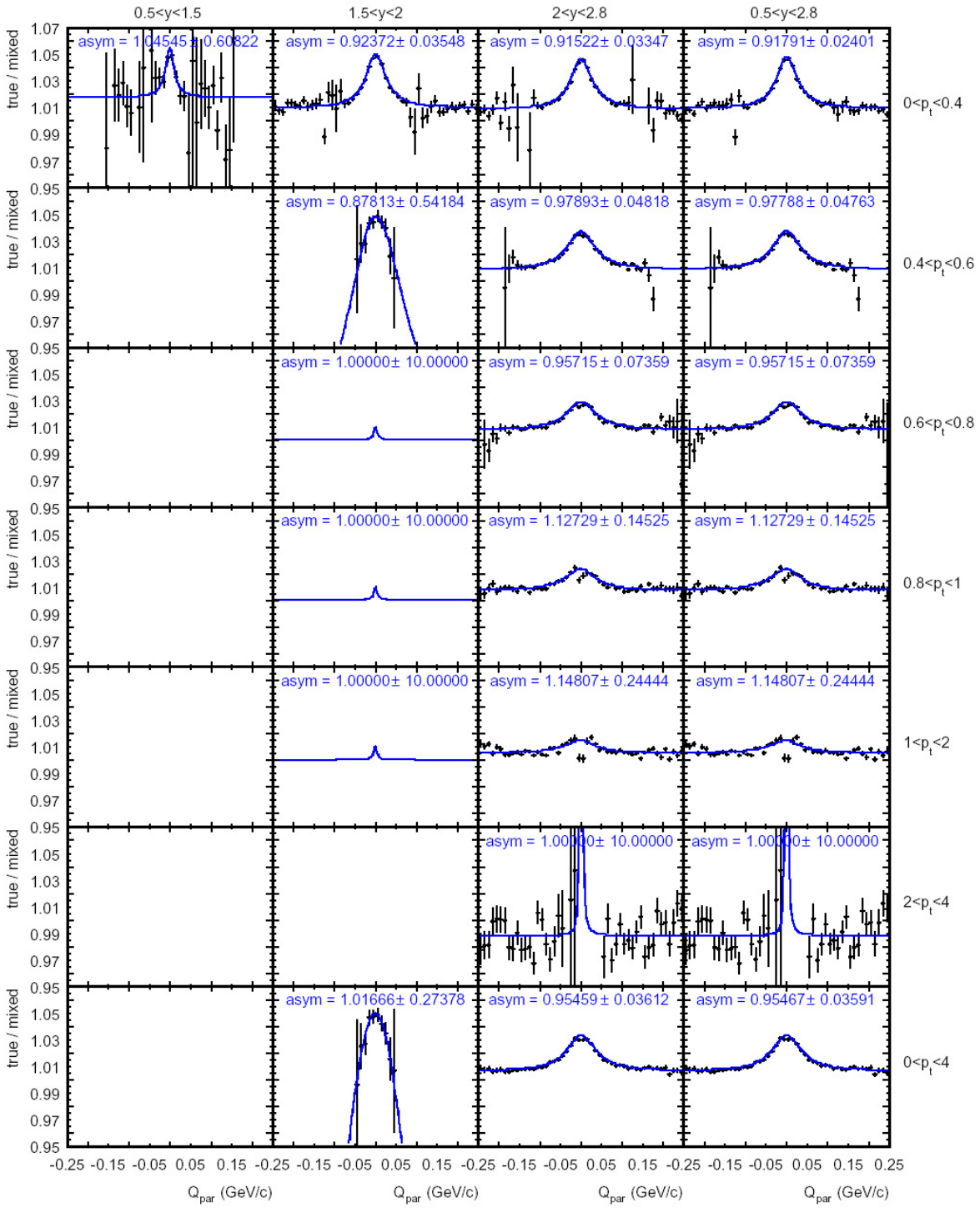

Figure B.1: The unlike-charge pion correlation functions.

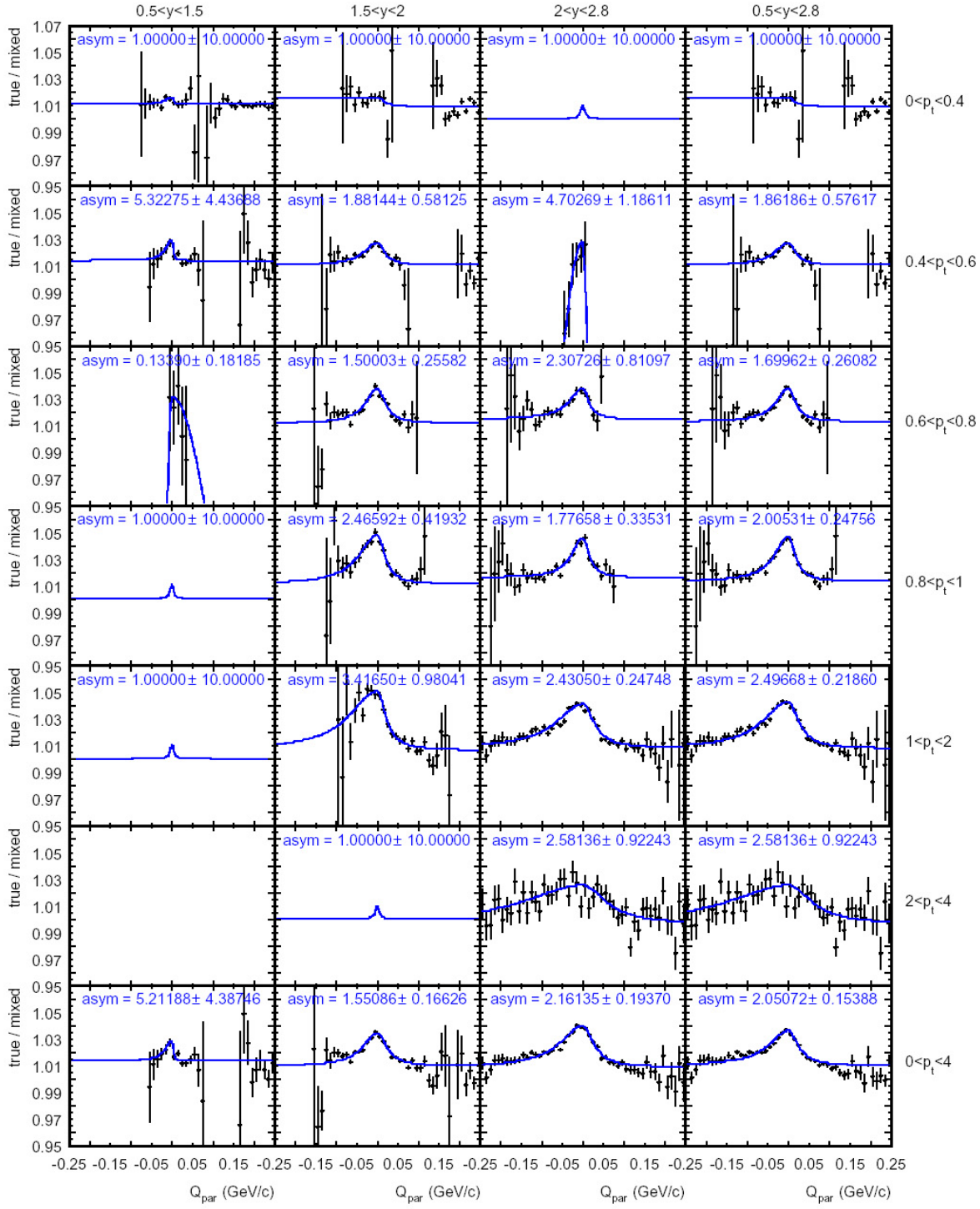

Figure B.2: The π^--p^+ correlation functions.

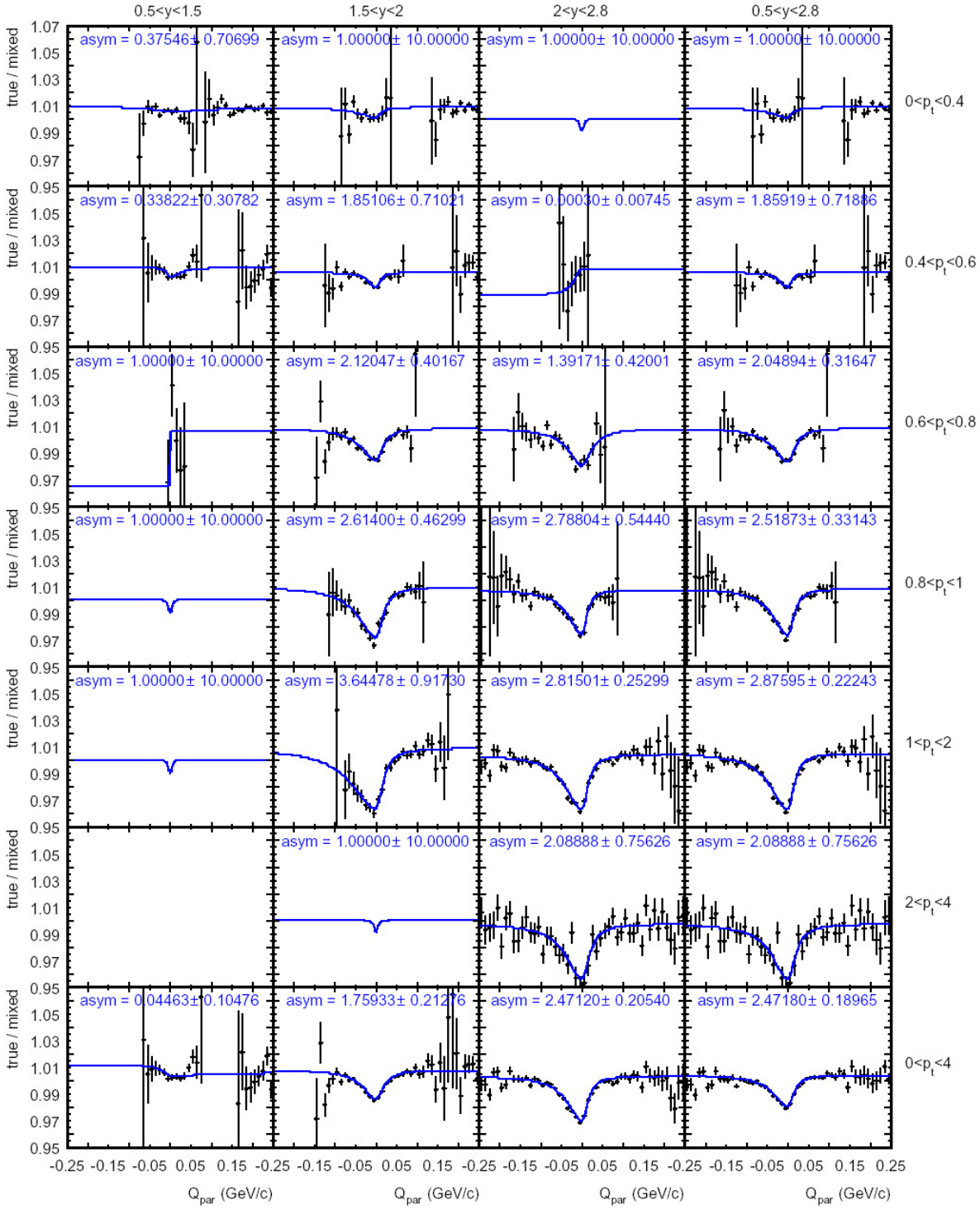

Figure B.3: The π^+-p^+ correlation functions.

Bibliography

[A+95] G. Agakichiev et al. Enhanced production of low mass electron pairs in 200 GeV/u S-Au collisions at the CERN SPS. *Phys. Rev. Lett.*, 75:1272–1275, 1995. 21

[A+96a] G. Agakichiev et al. Study of electron pair and photon production in Lead+Lead collisions at the CERN SPS; Addendum to proposal SPSLC/P280. Technical report, CERN/SPSLC 96-35, 1996. 30

[A+96b] G. Agakichiev et al. Thenical Note on the NA45/CERES Upgrade. Technical report, CERN/SPSLC 96-50, 1996. 30

[A+98a] G. Agakichiev et al. Neutral meson production in p-Be and p-Au collisions at 450 GeV beam energy. *Eur. Phys. J. C*, 4:249, 1998. 21

[A+98b] G. Agakichiev et al. Systematic study of low-mass electron pairs production in p-Be and p-Au collisions at 450 GeV/c. *Eur. Phys. J. C*, 4:231–247, 1998. 21

[A+03a] D. Adamova et al. Beam Energy and Centrality Dependence of Two-Pion Bose-Einstein Correlations at SPS Energies. *Nucl. Phys. A*, 714:124, 2003. xi, 96, 126, 127

[A+03b] A. Andronic et al. Pulse height measurements and electron attachment in drift chambers operated with Xe,CO2 mixtures. *Nucl. Instr. and Meth. Phys. Res. A*, 498:143, 2003. 40

[AAA+03] D. Adamova, G. Agakichiev, H. Appelshauser, V. Belaga, P. Braun-Munzinger, A. Castillo, A. Cherlin, S. Damjanovic, T.Dietel, L. Dietrich, A. Drees, S. I. Esumi, K. Filimonov, K.Fomenko, Z. Fraenkel, C. Garabatos, P. Glassel, G. Hering, J. Holeczek, V. Kushpil, B. Lenkeit, W. Ludolphs, A. Maas, A. Marin, J. Milosevic, A. Milov, D. Miskowiec, Yu. Panebrattsev, O. Petchenova, V. Petracek, A. Pfeiffer, J. Rak, I. Ravinovichand P. Rehak, H. Sako, W. Schmitz, J. Schukraft, S. Sedykh, S. Shimansky, J. Slivova, H. J. Specht, J. Stachel, M. Sumbera, H. Tilsner, I. Tserruya, J. P. Wessels, T. Wienold, B. Windelband,

J. P. Wurm, W. Xie, S. Yurevich, and V. Yurevich CERES Collaboration. Universal Pion Freeze-Out in Heavy-Ion Collisions. *Phys. Rev. Lett.*, 90(2):022301, 2003. 3

[AftSC04] J. Adams and for the STAR Collaboration. Identified particle distributions in pp and Au+Au collisions at $\sqrt{s_{NN}}$=200 GeV. *Phys. Rev. Lett.*, 92:112301, 2004. 134

[Ant04a] D. Antończyk. Production and monitoring of step3. *http://www-linux.gsi.de/ dantoncz/ceres/step3c/*, 2004. 62

[Ant04b] D. Antończyk. step2 – data quality monitoring. *http://www-linux.gsi.de/ dantoncz/ceres/monitoring/*, 2004. 60

[AS95] S. V. Akkelin and Yu. M. Sinyukov. The HBT-interferometry of expanding sources. *Phys. Lett. B*, 356(4):525–53, 1995. 13, 14

[B+87] R. Brun et al. GEANT3 – Detector Description and Simulation Tool. Technical report, CERN Report No. DD/EE/84-1, 1987. 59

[B+94] R. Baur et al. The CERES RICH detectors system. *Nucl. Instr. and Meth. Phys. Res. A*, 343:87–98, 1994. 26

[B+95] R. Baur et al. The pad readout of the CERES RICH detectors. *Nucl. Instr. and Meth. Phys. Res. A*, 355:329–341, 1995. 26

[B+97] J. Barrette et al. Proton and Pion Production Relative to the Reaction Plane in Au + Au Collisions at AGS Energies. *Phys. Rev. C*, 56:3254–3264, 1997. 74

[B+05] J. Y. Baud et al. User Guide for CASTOR. *http://it-dep-fio-ds.web.cern.ch/it-dep-fio-ds/Documentation/userguide.html*, 2005. 58

[Bar99] H. W. Barz. Combined effects of nuclear Coulomb field, radial flow, and opaqueness on two-pion correlations. *Phys. Rev. C*, 59(4):2214–2220, Apr 1999. 19

[Bay98] G. Baym. The physics of Hanbury Brown–Twiss intensity interferometry: from stars to nuclear collisions. *Acta Phys. Polon. B*, 29:1839, 1998. 18

[BBM96] G. Baym and P. Braun-Munzinger. Physics of Coulomb Corrections in Hanbury-Brown Twiss Interferometry in Ultrarelativistic Heavy Ion Collisions. *Nucl. Phys. A*, 610:286c, 1996. 17

[BC74] S. Baker and R. D. Cousins. Clarification of the use of chi-square and likelihood functions in fits to histograms. *Nucl. Instr. and Meth. Phys. Res.*, 221:472–474, 1974. 95

[Ber89] G. F. Bertsch. Pion interferometry as a probe of the plasma. *Nucl. Phys. A*, 498:173–179, Jul 1989. 15

[Bia99] S. F. Biagi. Monte Carlo simulation of electron drift and diffusion in counting gases under the influence of electric and magnetic fields. *Nucl. Instr. and Meth. Phys. Res. A*, 421:234–240, 1999. 43

[Bjo83] J. D. Bjorken. Highly relativistic nucleus-nucleus collisions: The central rapidity region. *Phys. Rev. D*, 27(1):140–151, 1983. 8

[BM00] P. Braun-Munzinger. Towards the Quark Gluon Plasma. *Nucl. Phys. A*, 663:183, 2000. v, 3, 4

[BMHS99] P. Braun-Munzinger, I. Heppe, and J. Stachel. Chemical equilibration in Pb+Pb collisions at the SPS. *Phys. Lett. B*, 465:15–20, 1999. 3

[BMMZ98] P. Braun-Munzinger, D. Miśkowiec, and P. Zimmermann. Laser calibration system for the CERES TPC. Technical report, GSI Scientific Report, 1998. 31

[BMS02] P. Braun-Munzinger and J. Stachel. Particle Ratios, Equilibration, and the QCD Phase Boundary. *J. Phys. G*, 28:1971, 2002. 3

[BMSWX96] P. Braun-Munzinger, J. Stachel, J. P. Wessels, and N. Xu. Thermal and hadrochemical equilibration in nucleus-nucleus collisions at the SPS. *Phys. Lett. B*, 365:1–6, 1996. 3

[Bow88] M. G. Bowler. Extended sources, final state interactions and Bose-Einstein correlations. *Z. Phys. C*, 39:81–88, 1988. 17

[Bow91] M. G. Bowler. Coulomb corrections to Bose-Einstein corrections have been greatly exaggerated. *Phys. Lett. B*, 270:69–74, 1991. 96

[BR] R. Brun and F. Rademakers. ROOT - An Object-Oriented Data Analysis Framework. *http://root.cern.ch*. 49

[BR94] W. Blum and L. Rolandi. *Particle Detection with Drift Chambers*. Springer-Verlag, 2nd edition, 1994. 29

[BR96] G. E. Brown and M. Rho. Chiral restoration in hot and/or dense matter. *Phys. Rep.*, 269(6):333–380, May 1996. 9

[BZS+99] M. Bleicher, E. Zabrodin, C. Spieles, S. A. Bass, C. Ernst, S. Soff, L. Bravina, M. Belkacem, H. Weber, H. Stocker, and W. Greiner. Relativistic Hadron-Hadron Collisions in the Ultra-Relativistic Quantum Molecular Dynamics Model (UrQMD). *J.PHYS.G*, 25:1859, 1999. 134

[CE02] CERN-EP/ED. ALICE TPC Readout Chip - User Manual. 2002. 51

[CL95] T. Csorgo and B. Lorstad. Bose-Einstein Correlations for Expanding Finite Systems. *Nucl. Phys. A*, 590:465c, 1995. 90

[CNH95] S. Chapman, J. R. Nix, and U. Heinz. Extracting source parameters from Gaussian fits to two-particle correlations. *Phys. Rev. C*, 52(5):2694–2703, 1995. 13

[Col00] E895 Collaboration. Azimuthal dependence of pion interferometry at the AGS. *Phys. Lett. B*, 496:1–8, 2000. 131

[Col04] STAR Collaboration. Azimuthally sensitive Hanbury Brown-Twiss interferometry in Au+Au collisions at $\sqrt{s_{NN}}$=200 GeV. *Phys. Rev. Lett.*, 93:012301, 2004. 120, 131

[CP75] J. C. Collins and M. J. Perry. Superdense Matter: Neutrons or Asymptotically Free Quarks? *Phys. Rev. Lett.*, 34(21):1353–1356, May 1975. 1, 2

[CSH95] S. Chapman, P. Scotto, and U. Heinz. New Cross Term in the Two-Particle Hanbury-Brown Twiss Correlation Function in Ultrarelativistic Heavy-Ion Collisions. *Phys. Rev. Lett.*, 74(22):4400–4403, May 1995. 14, 15, 16

[E$^+$04] S. Eidelman et al. Review of particle physics. *Phys. Lett.*, B592:1, 2004. 70

[EKL89] K. J. Eskola, K. Kajantie, and J. Lindfors. Quark and Gluon Production in High Energy Nucleus-Nucleus Collisions. *Nucl. Phys. B*, 323:37–52, 1989. 77

[EKO91a] J. Ellis, J. I. Kapusta, and K. A. Olive. Phase transition in dense nuclear matter with quark and gluon condensates. *Phys. Lett. B*, 273:123–127, Dec 1991. 1

[EKO91b] J. Ellis, J. I. Kapusta, and K. A. Olive. Strangeness, glue and quark matter content of neutrons stars. *Nucl. Phys. B*, 348:345–372, Jan 1991. 1

[G$^+$05] C. González Gutiérrez et al. The ALICE TPC Readout Control Unit. In *Proceeding of the 2005 IEEE Nuclear Science Symposium and Medical Imaging Conference*, Puerto Rico, 2005. 53

[Gar] C. Garabatos. Private communication. 41, 42

[Gar04] C. Garabatos. The ALICE TPC. *Nucl. Instr. and Meth. Phys. Res. A*, 535:197–200, 2004. vi, 34, 35, 36

[GGLP60] G. Goldhaber, S. Goldhaber, W. Lee, and A. Pais. Influence of Bose-Einstein Statistics on the Antiproton-Proton Annihilation Process. *Phys. Rev.*, 120(1):300–312, Oct 1960. 10

[GKW79] M. Gyulassy, S. K. Kauffmann, and L. Wilson. Pion interferometry of nuclear collisions. I. Theory. *Phys. Rev. C*, 20(6):2267–2292, Dec 1979. 18

[GL79] E. Gatti and A. Longoni. Optimum Geometry for Strip Cathodes or Grids in MWPC for Avalanche Localization Along the Andoe Wires. *Nucl. Instr. and Meth. Phys. Res. A*, 163:83–92, 1979. 41

[GM64] M. Gell-Mann. A schematic model of baryons and mesons. *Phys. Lett.*, 8:214–215, 1964. 2

[GM02] C. Garabatos and D. Miśkowiec. Electric field of CERES TPC. Technical report, GSI Scientific Report, 2002. 28

[GR84] E. Gatti and P. Rehak. Semiconductor Drift Chamber - An Application of a Novel Charge Transport Scheme. *Nucl. Instr. and Meth. Phys. Res. A*, 225:608–614, 1984. 24

[H+96] P. Holl et al. A 55 cm^2 cylindrical silicon drift detector. *Nucl. Instr. and Meth. Phys. Res. A*, 377:367–374, 1996. 25

[H+ 1] P. Holl et al. Study of Electron Pair and Photon Production in Lead+Lead Collisions at the CERN SPS. Technical report, CERN/SPSLC, 94-1. 21

[HB95] M. Herrmann and G. F. Bertsch. Source dimensions in ultrarelativistic heavy-ion collisions. *Phys. Rev. C*, 51(1):328–338, Jan 1995. 15, 126

[HBT56] R. Hanbury-Brown and R. Q. Twiss. Correlation between photons in two coherent beams of light. *Nature*, 177:27–29, 1956. 10

[Hei96a] U. Heinz. Hanbury-Brown/Twiss interferometry for relativistic heavy-ion collisions: Theoretical aspects. *nucl-th/9609029*, 1996. 12

[Hei96b] H. Heiselberg. Interferometry with Resonances and Flow in High-Energy Nuclear Collisions. *Phys. Lett. B*, 379:27, 1996. 90

[Her06] J. Castillo Hernandez. Development of a Ternary Mixture Monitor. Master's thesis, 2006. 54

[HHLW02] U. Heinz, A. Hummel, M. A. Lisa, and U. A. Wiedemann. Symmetry constraints for the emission angle dependence of Hanbury–Brown-Twiss radii. *Phys. Rev. C*, 66(4):044903, Oct 2002. 120, 131

[Ins] National Instruments. LabVIEW. *http:///www.ni.com/labview*. 49

[Joo05] M. Joos. Private communication. 2005. 53

[Jun05] A. Junique. Private communication. 2005. 50

[Kar02] F. Karsch. Lattice QCD at High Temperature and Density. *Lect. Note Phys.*, 583:209, 2002. 3

[KH03] P. F. Kolb and U. Heinz. Emission angle dependent HBT at RHIC and beyond. *Nucl. Phys. A*, 715:653–656, March 2003. 101

[KHHH01] P. F. Kolb, P. Huovinen, U. Heinz, and H. Heiselberg. Elliptic flow at SPS and RHIC: from kinetic transport to hydrodynamics. *Phys. Lett. B*, 500:232–240, 2001. 137

[KL03] F. Karsch and E. Laermann. Thermodynamics and in-medium hadron properties from lattice QCD. *hep-lat/0305025*, 2003. v, 3

[Kop74] G. I. Kopylov. Like particle correlations as a tool to study the multiple production mechanism. *Phys. Lett. B*, 50(4):472–474, 1974. 94

[KP71] G. I. Kopylov and M. I. Podgoretskii. Interference effects in two-resonance system. *Yad. Fiz.*, 14:1081–1090, 1971. 10

[KSH99] P. F. Kolb, J. Sollfrank, and U. Heinz. Anisotropic flow from AGS to LHC energies. *Phys. Lett. B*, 459:667, 1999. 137

[KSH00] P. F. Kolb, J. Sollfrank, and U. Heinz. Anisotropic transverse flow and the quark-hadron phase transition. *Phys. Rev. C*, 62(5):054909, Oct 2000. 101

[Lan53] L. D. Landau. On multiple production od particles during collisions of fast particles, English edition: Collected papers of L.D. Landau, D. Ter Haar ed., Pergamon, Oxford (1965). *Izv. Akad. Nauk. SSSR (Physics Series)*, 17:51, 1953. 7

[LD91] G. R. Lynch and O. I. Dahl. Approximations to multiple Coulomb scattering. *Nucl. Instr. and Meth. B*, 58:6–10, May 1991. 70

[Led04] R. Lednicky. Correlation femtoscopy of multiparticle processes. *YAD.FIZ.*, 67:73, 2004. 134

[Leo94] W. R. Leo. *Techniques for Nuclear and Particle Physics Experiments*. Springer-Verlag, 2nd edition, 1994. 39

[LHW00] M. A. Lisa, U. Heinz, and U. A. Wiedemann. Tilted pion sources from azimuthally sensitive HBT interferometry. *Phys. Lett. B*, 489:287–292, 2000. 119

[Lip00] C. Lippmann. Aufbau und Inbetriebnahme eines Gasqualitätsmonitors für die HADES-Driftkammern. Master's thesis, Institut für Kernphysik, Johann Wolfgang Goethe Universität, Frankfurt, 2000. 33

[LLEN96] R. Lednický, V.L. Lyuboshitz, B. Erazmus, and D. Nouais. How to measure which sort of particles was emitted earlier and which later. *Phys. Lett. B*, 373:30–34, 1996. 19, 105, 108

[Lud06] W. Ludolphs. *Measurement of Open Charm in 158 AGeV/c Pb-Au Collisions*. PhD thesis, Combined Faculties for the Natural Sciences and for Mathematics of the Ruperto-Carola University of Heidelberg, Germany, 2006. 58, 60

[LW74] T. D. Lee and G. C. Wick. Vacuum stability and vacuum excitation in a spin-0 field theory. *Phys. Rev. D*, 9(8):2291–2316, Apr 1974. 2

[Mar] A. Marin. Private communication. xii, 138

[Mat88] E. Mathieson. Cathode Charge Distributions in Multiwire Chambers: 4. Empirical formula for small anode-cathode separation. *Nucl. Instr. and Meth. Phys. Res. A*, 270:602–603, 1988. 41

[MAT89] QUARK MATTER. Proceedings of the 7th International Conference on Ultra-Relativistic Nucleus–Nucleus Collisions, Lenox, USA, 26-30 September, 1988. *Nucl. Phys. A*, 498, 1989. 1

[MAT04] QUARK MATTER. Proceedings of the 17th International Conference on Ultra-Relativistic Nucleus–Nucleus Collisions, Oakland, USA, 11-17 January, 2004. *J. Phys. G: Nucl. Part. Phys*, 30(8), 2004. 1

[MAT06] QUARK MATTER. Proceedings of the 18th International Conference on Ultra-Relativistic Nucleus–Nucleus Collisions, Budapest, Hungary, 4-9 August, 2005. *Nucl. Phys. A*, 774, August 2006. 1

[McL86] L. McLerran. The physics of the quark-gluon plasma. *Rev. Mod. Phys.*, 58(4):1021–1064, Oct 1986. 1

[Mer61] E. Merzbacher. *Quantum Mechanics*. Wiley & Sons, New York, 2nd edition, 1961. 18

[MftCC06] D. Miśkowiec and for the CERES Collaboration. Collection of CERES Results. *Nucl. Phys. A*, 774:43, 2006. 9

[Mil05] J. Miloŝević. *Investigation of Azimuthal Asymmetries in Charged and Strange Particle Distributions from CERES*. PhD thesis, Combined Faculties for the Natural Sciences and for Mathematics of the Ruperto-Carola University of Heidelberg, Germany, 2005. xii, 138

[MIN] MINUIT. CERN Program Library Long Writeup D506. 96

[Miś98] D. Miśkowiec. Separation between sources of pions and protons in central Au+Au collisions at the AGS (E877). *nucl-ex/9808003*, 1998. 19, 107

[Miś99] D. Miśkowiec. New trigger implementation for CERES/NA45 at CERN. Technical report, GSI Scientific Report, 1999. 23

[Miś00] D. Miśkowiec. Technical information about run 2000. *http://www-linux.gsi.de/ misko/ceres/daq/run-history-2000.txt*, 2000. 58

[Miś04] D. Miśkowiec. *Overlap* computer program. *http://www-linux.gsi.de/ misko/overlap*, 2004. 80

[Mor01] T. Morgan. Construction and Calibration of the STAR FTPC Drift Velocity Monitor. Technical report, Max-Planck-Institut für Physik (Werner-Heisenberg-Institut), 2001. 36

[MS88] A. N. Makhlin and Yu. M. Sinyukov. The hydrodynamics of hadron matter under a pion interferometric microscope. *Journal Zeitschrift für Physik C Particles and Fields*, 39(1):69–73, March 1988. 99, 126

[MT87] F. Mosteller and W. Tukey. *Data Analysis and Regression: A Second Course in Statistic*. Addison-Wesley, 1987. 59

[Mus05] L. Musa. Private communication. 2005. 50

[Oli91] K. A. Olive. The Quark - hadron transition in cosmology and astrophysics. *Science*, 251:1194–1199, 1991. 1

[Oll92] J. Y. Ollitrault. Anisotropy as a signature of transverse collective flow. *Phys. Rev. D*, 46(1):229–245, Jul 1992. 101

[Oll95] J. Y. Ollitrault. Collective flow from azimuthal correlations. *Nucl. Phys. A*, 590:561c–564c, 1995. 72

[Oll97] J. Y. Ollitrault. Reconstructing azimuthal distributions in nucleus-nucleus collisions. *arXiv:nucl-ex/9711003*, 1997. viii, 74, 75, 79

[Oll98] J. Y. Ollitrault. Flow systematics from SIS to SPS energies. *Nucl. Phys. A*, 638:c195–c206, August 1998. 102

[Pol78] A. M. Polyakov. Thermal properties of gauge fields and quark liberation. *Phys. Lett. B*, 72:477–480, 1978. 1, 2

[Pot96] K. M. Potter. The Large hadron Collider (LHC) project of CERN. Technical report, CERN LHC Project Report 36, 1996. 33

[Pra84] S. Pratt. Pion Interferometry for Exploding Sources. *Phys. Rev. Lett.*, 53(13):1219–1221, Sep 1984. 99

[Pra86a] S. Pratt. Coherence and coulomb effects on pion interferometry. *Phys. Rev. D*, 33(1):72–79, Jan 1986. 18

[Pra86b] S. Pratt. Pion interferometry of quark-gluon plasma. *Phys. Rev. D*, 33(5):1314–1327, Mar 1986. 15

[PS75] V. Palladino and B. Sadoulet. The ALICE TPC. *Nucl. Instr. and Meth.*, 128:323–335, 1975. 35

[PV98] A. M. Poskanzer and S. A. Voloshin. Methods for analyzing anisotropic flow in relativistic nuclear collisions. *Phys. Rev. C*, 58:1671–1678, 1998. viii, 74, 76, 79

[Rad06] S. Radomski. PhD thesis, TECHNISCHE UNIVERSITÄT DARMSTADT, 2006. xii, 138

[RC04] C. P. Robert and G. Casella. *Monte Carlo Statistical Methods*. Springer-Verlag New York Inc., 2nd edition, 2004. 113

[RftSC03] F. Retiere and for the STAR Collaboration. Non-identical particle correlation analysis as a probe of transverse flow. *Nucl. Phys. A*, 715:591, 2003. 105

[RL04] F. Retiere and M. A. Lisa. Observable implications of geometrical and dynamical aspects of freeze-out in heavy ion collisions. *Phys. Rev. C*, 70(4):044907, 2004. 19, 138

[RW00] R. Rapp and J. Wambach. Chiral symmetry restoration and dileptons in relativistic heavy-ion collisions. *Adv. Nucl. Phys.*, 25:1–205, 2000. 9

[S$^+$98] Yu. M. Sinyukov et al. Coulomb corrections for interferometry analysis of expanding hadron systems. *Phys. Lett. B*, 432:248–257, 1998. 96

[Sch98] W. Schmitz. Cathode pad design for the CERES-TPC. Technical report, CERES-Note, 1998. 30

[Shu73] E. V. Shuryak. The correlations of identical pions in multibody production. *Phys. Lett. B*, 44(4):387–389, 1973. 10

[Shu78] E. V. Shuryak. Quark-gluon plasma and hadronic production of leptons, photons and psions. *Phys. Lett. B*, 78:150–153, 1978. 1

[Slı03] J. Slıvová. *Azimuthal Correlations of High-pt Pions in 158 AGeV/c Pb-Au Collisions Measured by the CERES Experiment*. PhD thesis, Charles University in Prague, Faculty of Mathematics and Physics, 2003. 25, 113

[SP71] R. M. Sternheimer and R. F. Peierls. General Expression for the Density Effect for the Ionization Loss of Charged Particles. *Phys. Rev. B*, 3(11):3681–3692, Jun 1971. 66

[Sta99] J. Stachel. Towards the Quark-Gluon Plasma. *Nucl. Phys. A*, 654:119c, 1999. 3

[SVA96] Y. M. Sinyukov S. V. Akkelin. The HBT-interferometry of expanding inhomogeneous sources. *Z. Phys. C*, 72:501–507, 1996. 134

[Til02] H. Tilsner. *Two-Particle Correlations at 40, 80, and 158 AGeV Pb-Au Collisions*. PhD thesis, Combined Faculties for the Sciences and for Mathematics of the Ruperto-Carola University of Heidelberg, Germany, 2002. 31

[TLS01] D. Teaney, J. Lauret, and E. V. Shuryak. A Hydrodynamic Description of Heavy Ion Collisions at the SPS and RHIC, 2001. 101

[TPC01] TPC Technical Design Report. Technical report, CERN/LHCC, 2000-001. 33

[TWH00] B. Tomasik, U. A. Wiedemann, and U. Heinz. Dynamics and Sizes of the Fireball at Freeze-out. *Nucl. Phys. A*, 663:753, 2000. 99

[VC96] S. A. Voloshin and W. E. Cleland. Hanbury-Brown–Twiss analysis of anisotropic transverse flow. *Phys. Rev. C*, 53(2):896–900, Feb 1996. 16

[Vee98] R. Veenhof. Garfield, recent developments. *Nucl. Instr. and Meth. Phys. Res. A*, 419:726–730, 1998. 39

[Vee03] R. Veenhof. Choosing a gas mixture for the ALICE TPC. Technical report, CERN/TPC ALICE-INT-2003-29, 2003. 34

[VZ96] S. Voloshin and Y. Zhang. Flow Study in Relativistic Nuclear Collisions by Fourier Expansion of Azimuthal Particle Distributions. *Z. Phys. C*, 70:665–671, 1996. 10, 72

[Wei00] R. M. Weiner. Boson Interferometry in High Energy Physics. *Phys. Rep.*, 327:249, 2000. 17

[WH97] U. A. Wiedemann and U. Heinz. Resonance contributions to Hanbury-Brown Twiss correlation radii. *Phys. Rev. C*, 56(6):3265–3286, Dec 1997. 90

[WH99] U. A. Wiedemann and U. Heinz. Particle Interferometry for Relativistic Heavy-Ion Collisions. *Phys. Rep.*, 319:145, 1999. 12, 126

[Wie98] U. A. Wiedemann. Two-particle interferometry for noncentral heavy-ion collisions. *Phys. Rev. C*, 57(1):266–279, Jan 1998. 16, 99

[WSH96] U. A. Wiedemann, P. Scotto, and U. Heinz. Transverse momentum dependence of Hanbury-Brown–Twiss correlation radii. *Phys. Rev. C*, 53(2):918–931, Feb 1996. 99

[WW02] B. A. Weaver and A. J. Westphal. Energy loss of relativistic heavy ions in matter. *Nucl. Instr. and Meth. B*, 187:285–301, 2002. 40, 66

[Yur06] S. Yurevich. *Electron-Pair Production in 158 AGeV/c Pb-Au Collisions from CERES*. PhD thesis, Combined Faculties for the Natural Sciences and for Mathematics of the Ruperto-Carola University of Heidelberg, Germany, 2006. 58, 59, 62, 67, 113

[ZBB+84] W. A. Zajc, J. A. Bistirlich, R. R. Bossingham, H. R. Bowman, C. W. Clawson, K. M. Crowe, K. A. Frankel, J. G. Ingersoll, J. M. Kurck, C. J. Martoff, D. L. Murphy, J. O. Rasmussen, J. P. Sullivan, E. Yoo, O. Hashimoto, M. Koike, W. J. McDonald, J. P. Miller, and P. Truöl. Two-pion correlations in heavy ion collisions. *Phys. Rev. C*, 29(6):2173–2187, Jun 1984. 19

[Zie98] J. F. Ziegler. The stopping and range of ions in matter. *http://www.srim.org/*, 1998. 41

Acknowledgements

This work would have not been possible without the effort and involvement of many people to whom I would like to express my gratitude. I am deeply grateful to Prof. Dr. P. Braun-Munzinger for giving me the opportunity to join his research groups and introducing me as a member of the CERES and the ALICE collaborations. For all these years I have learnt much from him. I appreciate his interest of my work as well as many valuable suggestions for improving the work. Dr. D. Miśkowiec deserves a special mention, his enthusiasm and experience helped me to make the research interesting and enjoyable. Since the very beginning he has guided me with patience through the beautiful field of the two-particle correlations. I express also many thanks to Dr. C. Garabatos who introduced me into the physics of gaseous detectors. He give me a unique opportunity to extend my knowledge about the complex systems used for developing modern physics detectors. I am also very grateful to Prof. Dr. J. Stachel for her useful suggestions. I want to show my appreciation of all the members of the CERES and the ALICE collaborations, especially to Prof. Dr. Harald Appelshäuser and Dr. A. Marin for their comments and suggestions during all these years. I would like to thanks to Pasi Huovieni for providing me with the hydrodynamical calculation. A special thanks to my office mate Oliver Busch for all discussions about physics and great working atmosphere. There are no words which will express how much I thanks to my girlfriend Katarzyna. Finally, I would like to thank all my friends. Last but not least, not to forget my family for all their support and encouragement they have given me throughout my education.

Curriculum Vitae

Personal Data

Name	Dariusz
Surname	Antończyk
Place of Birth	Kraków
Date of Birth	03 December 1976
Marital Status	single
Nationality	polish

Education

10/2002 - 10/2006	Doctoral fellowship at the Gesellschaft für Schwerionenforschung and preparation of the dissertation
09/1997 - 10/2002	M.Sc. of Physics, Institute of Physics of the Jagiellonian University in Kraków, Poland Main subject: Experimental Particle Physics Thesis: Client/server software for controlling a low voltage power supply in ATLAS TRT

Publications

1. *Latest results on e+ e- pair production in CERES*, Nucl. Phys. A749, 160-165 (2005)
2. *Leptonic and Charged Kaon Decay Modes of the ϕ Meson Measured in Heavy-Ion Collisions at the CERN Super Proton Synchrotron*, Phys. Rev. Lett. 96, 152301 (2006)

3. *Performance studies with an ALICE TPC prototype*, Nucl. Inst. Meth. A565, 2, 551-560 (2006)

4. *Non-identical particle correlation in central Pb+Au collisions at 158 A GeV*, Nukleonika 51, Supplement 3, 47-50 (2006)

Presentations

1. *Two-particle correlations in Pb+Au collisions at 158 AGeV*, DPG Tagung, Köln, 2004

2. *Non-identical particle correlations in central Pb+Au collisions at 158 GeV per nucleon*, V-I Workshop on 'Physics of strongly interacting matter at high densities' Bad Liebenzell, 3-5 October 2005

3. *Two-particle correlations in Pb+Au collisions at 158 AGeV*, DPG Tagung, München, 2006

Erklärung

Hiermit erkläre ich an Eides statt, daß ich die vorliegende Dissertation selbständig verfaßt, keine anderen als die angegebenen Hilfsmittel verwendet und noch keinen Promotionsversuch unternommen habe.

Darmstadt, den 15. Okt 2006,

gez. Dariusz Antończyk.

_____

Unterschrift